nature communications

Article

https://doi.org/10.1038/s41467-026-69979-9

Pharmacological stabilization of hypoxia-inducible factor 1-α dampens the interferon response and promotes glycolysis in Aicardi-Goutières syndrome

Received: 4 November 2025

Accepted: 11 February 2026

Published online: 03 March 2026

Check for updates

Maxime Batignes[1,2] ✉, Marine Luka[1,2,3,13], Surabhi Jagtap[1,2,13], Camille de Cevins[1,2,13], Ivan Nemazanyy[4], Jacqueline Leib[1,2], Tinhinane Fali[1,2,5], Alexandre Pierga[1,6], Mohammed Zarhrate[7], Víctor García-Paredes[1,2], Francesco Carbone[1,3], Brieuc P. Pérot[1,2], Bénédicte Neven[8], Brigitte Bader-Meunier[8], Pierre Quartier[8], Marie Hully[9], Alexandre Belot[10,11], Alice Lepelley[1,6], Marie-Louise Frémond[1,6,8], Alain Fischer[8,12] & Mickaël M. Ménager[1,2,3] ✉

Aicardi-Goutières syndrome (AGS) is a genetic type I interferon (IFN)-mediated disease characterized by neurological involvement with onset *in utero* or in childhood. Here, we analyze peripheral blood samples from patients bearing AGS-causing mutations in *ADAR1, RNASEH2B* or *SAMHD1* using single-cell transcriptomics and targeted metabolomics. Using machine-learning approaches and differential gene expression analysis, we identified a loss of transcription factor hypoxia induced factor 1 α (HIF-1α) expression and activity associated with features of a metabolic switch favoring oxidative phosphorylation and glutathione metabolism over glycolysis in monocytes and dendritic cells. Evidences of mitochondrial stress and accumulation of cytosolic double-stranded DNA and RNA were also found. The energy metabolic switch was confirmed at the metabolic level in primary peripheral blood mononuclear cells of AGS patients. Chemical stabilization of HIF-1α using a synthetic drug in in vitro cellular models of AGS, reversed the energy metabolic switch towards glycolysis, attenuated mitochondrial stress, and markedly reduced the IFN response and IP-10 production. We therefore propose that an energy metabolic switch contributes to chronic inflammation in AGS and that targeting this pathway might represent a potential therapeutic approach.

Aicardi-Goutières syndrome (AGS) is a monogenic disorder with onset frequently observed in utero or in the first months of life. Mutations causing AGS have been identified in genes encoding the exonuclease TREX1 (AGS1)[1], the components B, C and A of the RNase H2 complex (RNASEH2B (AGS2), RNASEH2C (AGS3), RNASEH2A (AGS4))[2], the deoxynucleotide triphosphate triphosphohydrolase SAMHD1 (AGS5)[3], the double-stranded RNA-specific adenosine deaminase ADAR1 (AGS6)[4], the cytosolic double-strand (ds)RNA sensor IFIH1 (AGS7)[5] and components of the replication-dependent histone pre-mRNA-processing complex LSM11 (AGS8) and RNU7-1 (AGS9)[6]. The encoded proteins are involved in the processing (AGS1-6) or sensing (AGS7-9) of cellular nucleic acid, and disruption of their normal function can

A full list of affiliations appears at the end of the paper. ✉e-mail: maxime.batignes@institutimagine.org; mickael.menager@institutimagine.org

induce an aberrant and chronic antiviral transcriptomic response (Table 1)[7]. These sensing pathways can be separated into two arms: on the one hand, detection of dsDNA and RNA/DNA hybrids leads to the activation of the stimulator of interferon genes (STING) pathway; on the other hand, dsRNA sensing triggers mitochondrial antiviral-signaling protein (MAVS). Both STING and MAVS activation converge on the activation by phosphorylation and nuclear translocation of the transcription factor IRF3, leading to the production of type I interferon (IFN) and the induction of cell defense mechanisms against viruses[8].

Mutations described in AGS lead to constitutive triggering of the nucleic acid sensing pathways and the production of type I IFN, even in the absence of any viral infection[6,9]. Thus, AGS is a chronic, inflammatory disorder that can mimic *in utero*-acquired viral infection but differs, notably, in the type and nature of cytokines produced. In AGS, the inflammatory response is orchestrated by type I IFN signaling but also involves inflammatory signals through IFN-induced protein 10 (IP-10, also called CXCL10), with no obvious upregulation of interleukin (IL)−6 or IL-8 as typically observed in response to viruses[10]. The major clinical features of AGS relate to the brain, most particularly intracranial calcification, white matter disease and cerebral atrophy. Extra-neurological involvement can also occur, including vasculitis chilblain-like lesions, and features consistent with systemic lupus erythematosus (SLE) in some cases[9].

While type I IFN protein levels can be difficult to measure in patients, its activity can be monitored by following the expression of IFN-stimulated genes (ISG) such as IP-10, whose concentration levels are consistently elevated both in serum and the cerebrospinal fluid of AGS patients[10]. Importantly, the type I IFN response and IP-10 have been shown to induce direct neurotoxicity in humans[11]. The use of type I IFN targeted therapies in AGS, namely JAK/STAT inhibitors, has been proven to be efficient in reducing type I IFN production but with limited effects on neurologic involvement and also favoring opportunistic infections[12,13], arguing for a need to identify alternative therapeutic targets in AGS. In the present study, we screened peripheral blood mononuclear cells (PBMC) from patients with AGS using single cell RNA sequencing (scRNA-seq), targeted metabolomic and validated our findings in in vitro models for AGS to reveal potentially new cellular mechanisms relevant to the pathogenesis.

Results

Marked changes in metabolic pathways associated to type I IFN response and inflammation in AGS

First, to investigate the transcriptomic profile of AGS patients' cells, two single-cell RNA-sequencing (scRNA-seq) experiments were performed, by using the Cellular Indexing of Transcriptomes and Epitopes by Sequencing (CITE)-seq method[14]. PBMC of 6 AGS patients, carrying biallelic loss of function mutations in 3 different genes were analyzed: *RNASEH2B* gene (AGS2: P1 and P2); *ADAR1* gene (AGS6: P3 and P4); *SAMHD1* (AGS5: P7 and P8). PBMCs from 2 patients with a dominant-negative mutation in *COPA* gene (COPA: P5 and P6) were added as controls of a type I IFN-driven disease mediated through chronic STING activation even in the absence of direct aberrant nucleic acid sensing[15]. PBMC from unrelated healthy individuals were used as controls (CTRL: C1 to C5). No batch effect related to age and sex were detected following quality control, filtering and integration of the samples. A 5-fold and a 7-fold increase in the median number of features (genes) and counts per cell were observed respectively, between the two independent single-cell experiments, due to the use of two different chemistry (10x chemistry v3 for library generation for the AGS2/AGS6/COPA dataset and 10x chemistry v2 for the AGS5 dataset). Therefore, to avoid potential batch effects, AGS5 and AGS2/AGS6/COPA patients' data were integrated and analyzed independently (figure S1A–S1D). Cell types were annotated based on a combination of markers and signature scores as previously described[16] (figure S1C and S1D).

IFN-stimulated gene (ISG) expression at the single-cell transcriptomic level, was first assessed using a previously described signature of 272 ISG designed for transcriptomic analysis[17]. As expected, an elevated type I IFN signature was observed in AGS2, AGS6 and AGS5 patients compared to CTRL, with COPA patients presenting an intermediate state (Figs. 1A, B). We noticed that type I IFN response was higher in monocytes/conventional dendritic cells (cDC) compared to other macroclusters of PBMC in all patients (Figs. 1C, D). Differences in cell type proportions were also analyzed (figure S1E and S1F). Although only 2 unrelated patients for each genotype were assessed, an increase in the ratio of T naïve / T memory and a decrease in MAIT and Tγδ cells in all AGS patients were seen (figure S1E and S1F). These changes are reminiscent to proportions reported in other type I IFN-related diseases such as SAVI[16] or severe COVID-19[18]. In addition, an increase in B cells, particularly in AGS2 patients, and a decrease in the monocytes/cDC compartment in ASG6 patients were measured (figure S1E). For differential gene expression (DEG) analyses, cells were next grouped in macroclusters according to the major cell types found in PBMC (figure S1G and S1H).

A DEG analysis was then performed on all PBMC, as well as all macroclusters (monocytes/cDC, B cells, CD4 T cells, CD8 T cells, NK/MAIT/Tγδ, pDC of AGS patients compared to CTRL samples and pathway enrichment on DEG was estimated using ingenuity pathway analysis (IPA QUIAGEN)[19]. As expected, type I IFN responses (Interferon alpha_beta signaling) was found to be upregulated in AGS (Fig. 1E, F) and was associated with inflammatory responses and immune cell cycle pathways in all macroclusters, indicative of an active immune

Table 1 | AGS subtypes

AGS subtype	Gene	Mutations	Role in nucleic acid pathway	Type I IFN signaling
AGS1	TREX1	LOF	DNA-RNA/DNA hybrid degradation	STING/IRF3
AGS2	RNASEH2B	LOF	RNA/DNA hybrid degradation	STING/IRF3
AGS3	RNASEH2C	LOF	RNA/DNA hybrid degradation	STING/IRF3
AGS4	RNASEH2A	LOF	RNA/DNA hybrid degradation	STING/IRF3
AGS5	SAMHD1	LOF	Prevent cytosolic retro-transcription/sequesters RNA	STING/IRF3
AGS6	ADAR1	LOF	RNA editing	MAVS/IRF3
AGS7	IFIH1	GOF	RNA sensing	MAVS/IRF3
AGS8	LSM11	LOF	DNA sensing	STING/IRF3
AGS9	RNU7-1	LOF	DNA sensing	STING/IRF3

Mutations in 9 AGS causing genes have been Identified leading to the establishment of 9 disease subtypes (AGS1-AGS9). Mutations can be a loss of function mutations (LOF) or a gain of function mutations (GOF). Mutations associated with AGS favor accumulation and sensing of RNA and DNA structures inducing respectively STING and MAVS adaptors, followed by IRF3 and type I IFN chronic activation. AGS: Aicardi-Goutières syndrome, TREX1: Three Prime Repair Exonuclease 1, RNASEH2B-C-A: components B, C and A of the RNase H2 complex, ADAR1: Adenosine Deaminase RNA Specific, IFIH1: Interferon Induced with Helicase C Domain 1, RNU7-1: RNA, U7 Small Nuclear 1, STING: stimulator of interferon genes, MAVS: mitochondrial antiviral-signaling protein, IRF3: Interferon Regulatory Factor 3.

https://doi.org/10.1038/s41467-026-69979-9

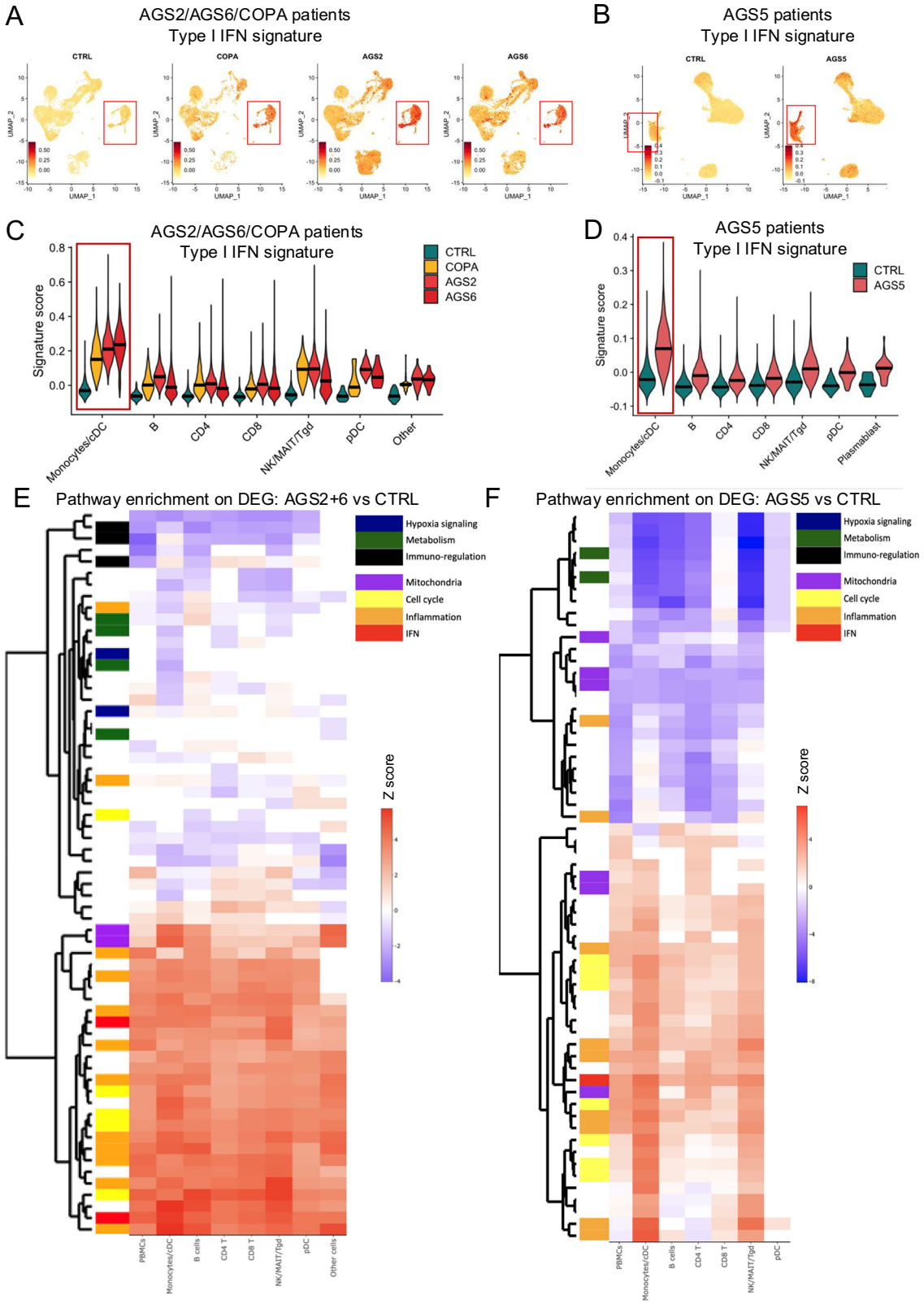

system. Genes involved in mitochondrial activity (electron transport chain, oxidative phosphorylation, mitochondrial translation) were also highly enriched in AGS patients. Downregulated pathways in AGS notably included immune regulation, hypoxia signaling and metabolic pathways (Fig. 1E, F).

Overall, scRNA-seq analyses performed on PBMC of AGS patients, suggested an interesting link between type I IFN mediated inflammation and metabolism with the strongest type I IFN response observed in monocytes/cDC.

Gene regulatory network analysis inferred a loss of HIF-1α transcription factor activity of AGS patients' PBMC

To obtain an unsupervised understanding of factors driving the observed transcriptomic profiles in AGS, a gene regulatory network

Fig. 1 | Transcriptomic profile of PBMC from AGS patients. A scRNA-seq Data from PBMC of two patients with a mutation in *RNASEH2B* gene (P1 and P2), two patients with a mutation in *ADAR1* gene (P3 and P4) and two patients with a mutation in *COPA* gene (P5 and P6) were labeled as AGS2, AGS6 and COPA groups, respectively. None of the patients were related and their data were integrated with data from PBMC of two unrelated healthy controls (CTRL group: C1 and C2) to generate the AGS2/AGS6/COPA integration. None of the patients were under immunosuppressive or reverse transcriptase inhibitors (RTI) therapy at the time of sampling. Color scale represents feature plot of type I IFN signature (signature of 272 genes upregulated following type I IFN signaling). Red squares focus on monocytes/cDC macrocluster. **B** scRNA-seq Data from PBMC of two patients developing AGS with a mutation in *SAMHD1* gene (P7 and P8), were labeled as group AGS5. P8 was under 5 months of reverse transcriptase inhibitors tri-therapy (RTI). P7 was sampled before and after 1 month of RTI treatment. Patients scRNA-seq data were integrated with data from PBMC of 3 unrelated healthy donors C5, C6 and C7 (CTRL group) to generate the AGS5 integration. Feature plot of type I IFN signature score (signature of 272 genes upregulated following type I IFN signaling) is represented. Red squares indicate monocytes/cDC macrocluster. Color scale indicates signature score. **C** Violin plot of type I IFN signature score on the AGS2/AGS6/COPA integration. Red square highlights monocytes/cDC macrocluster. **D** Violin plot of type I IFN signature score on the AGS5 integration. Red square highlights monocytes/cDC macrocluster. **E**, **F** Heatmap of top 10 downregulated pathways (blue color) and top 10 upregulated pathways (red color) among DEG between AGS and CTRL groups for every macroclusters and whole PBMC of AGS2/AGS6/COPA integration (**E**) and AGS5 integration (**F**). Color scale indicates Z-score for each pathway. Pathway enrichment was performed using ingenuity pathway analysis (IPA)(Quiagen). cDC= classical Dendritic cells; B = B lymphocytes; CD8 T= Lymphocytes T $CD8^+$; CD4 T= Lymphocytes T $CD4^+$; NK= Natural Killer cells; MAIT= Mucosal-associated invariant T cells; Tγδ= Lymphocytes Tγδ; pDC= plasmacytoid dendritic cells.

(GRN) analysis[20] was performed by applying pySCENIC (Single-Cell rEgulatory Network Inference and Clustering)[20] to the scRNA-seq data sets. GRN allowed to identify the transcription factors most likely to be relevant to the transcriptomic profiles of PBMC in CTRL and AGS patients separately (figure S2A and S2C). Briefly, co-expression modules were generated using GRNboost[21] to associate transcription factors (TF) that share pattern of expression with other genes. Presence of TF binding motifs were evaluated for each gene using RcisTarget. Only genes that present the binding motif of the associated TF were kept in the final network.

To estimate changes in the activities of TFs between CTRL and AGS patients' PBMC, a differential analysis was performed for each TF, calculating the ratio of its number of inferred targets in the AGS condition to its number of inferred targets in the control condition (Fig. 2A, C). Several of the TFs with increased number of targets expression in AGS patients PBMC were related to type I IFN responses involving factors such as IRF8, IRF7, PRDI-BF1 (*PRDM1*) and STAT1. In contrast, in both datasets, HIF-1α (encoded by *HIF1A*) stood out as the TF with the most important loss of inferred number of target genes expression in AGS compared to the CTRL group, (Figs. 2A, C, S2B and S2D). Analysis of the number of inferred targets was then compared with the differential mRNA expression of each TF. Expression of the top TFs in CTRL, including HIF1A, CEBPD, FOS and CEBPD, was particularly downregulated in monocytes/cDC of all AGS patients (Figs. 2B, D) but a combined reduction of expression and decrease of the number of inferred targets was only observed for HIF1A.

Thus, unsupervised approaches, with GRN analyses, pointed towards a major downregulation of HIF-1α activity and expression most noticeable in the monocytes/cDC compartment of AGS patients.

Exacerbated oxidative phosphorylation and mitochondrial stress were associated with defective HIF-1α transcriptional program in monocytes/cDC of AGS patients

Preliminary analysis using DEG on all subpopulations (Figs. 1E, F) and differential TF expression and activity (Fig. 2B, D) pointed out to particular transcriptomic modifications in monocytes/cDC alongside the highest response to type I IFN (Figs. 1A, B). Pathway enrichment was consequently specifically addressed in monocytes/cDC based on DEG between AGS and CTRL using EnrichR software[22].

Besides an increased type I IFN response and a downregulation of HIF-1α activity, an upregulation of oxidative phosphorylation, mitochondrial activity and a decrease in glycolysis were observed in AGS' monocytes/cDC (Figs. 3A, 3B, S3A and S3B) in conjugation with a decrease of HIF-1α expression (figure S3C and S3D). HIF-1α, encoded by *HIF1A*, is a sensor of energy metabolism stress, it regulates energy production pathways, orienting glucose consumption through anaerobic glycolysis instead of oxidative phosphorylation[23,24]. Signature scores from a curated list of genes categorized as HIF-1α targets, or associated to oxidative phosphorylation and glycolysis pathways were then specifically assessed (table S2) on the monocyte/cDC macrocluster. A 3-fold lower median HIF-1α target expression in AGS2 and AGS6 patients' monocytes/cDC compared to CTRL, together with a mild increase of oxidative phosphorylation and 2-fold decrease in glycolysis scores were noticed (Fig. 3C) and confirmed our pathways enrichment analyses. High expression level of genes involved in oxidative phosphorylation led to search for features of mitochondrial stress in transcriptomic data (Supplementary Data 2 [25–30]). An 8-fold higher expression of mitochondrial stress genes was measured in monocytes/cDC of AGS2 and AGS6 patients as compared to CTRL (Fig. 3C). Similar results were obtained in AGS5 patients' cells (Fig. 3D and S3F). In COPA patients, an intermediate level of HIF1A expression, HIF1A targets, oxidative phosphorylation, glycolysis scores and mitochondrial stress was noticed (Fig. 3C) alongside the intermediate level of type I IFN response (Fig. 1A).

Collectively, the combination of a supervised approach using pathway enrichment on DEG, and an unsupervised approach using machine learning on GRN to infer TF activity from the scRNAseq dataset, both pointed to defective HIF-1α transcription factor activity in monocytes/cDC of AGS patients. Loss of HIF-1α activity was associated with features of a metabolic switch involving defective anaerobic glycolytic capacity and excessive oxidative phosphorylation together with mitochondrial stress, particularly in monocytes/cDC compartment (figure S3E and S3F).

Similar type I interferon response, energy metabolic switch and mitochondrial stress are found in in vitro cellular models of AGS

To validate the observations drawn from scRNA-seq analysis of AGS patients' PBMC, three in vitro cellular models, based on primary monocytes from healthy blood donors differentiated into dendritic cells (MDDC, monocyte derived dendritic cells) were established. In these models, either *SAMHD1, ADAR* and *RNASEH2B* genes were targeted with short hairpin RNA (shRNA) to replicate loss of function observed in AGS5, AGS2 and AGS6 patients respectively (Fig. 4A). shRNA efficiently inhibited *SAMHD1, ADAR* and *RNASEH2B* genes expression at the mRNA level (figure S4A), while also inducing a noticeable downregulation at the protein level (figure S4B–4D). Upon knock-down (KD) of these 3 genes, detectable amounts of IFN-β protein and high amounts of IP-10 were measured (Fig. 4B and S4E), but not IL-1β nor TNFα, consistent with what has been reported in AGS patients[10]. A strong type I IFN response, was also observed, monitoring ISG15 expression by flow cytometry (Fig. 4C and S4F) and qRT-PCR of 6 ISG used in clinical routine practice[31] (*ISG15, IFI44L, IFIT1, IFI27, RSAD2* and *SIGLEC1*) (Fig. 4D).

Pathway enrichment in differentially expressed genes (DEG) in AGS MDDC models, following bulk RNA-seq, confirmed engagement of a type I IFN transcriptomic program in AGS models, compared to MDDC transduced with a control shRNA (scr) (Fig. 4E **left**) together

https://doi.org/10.1038/s41467-026-69979-9

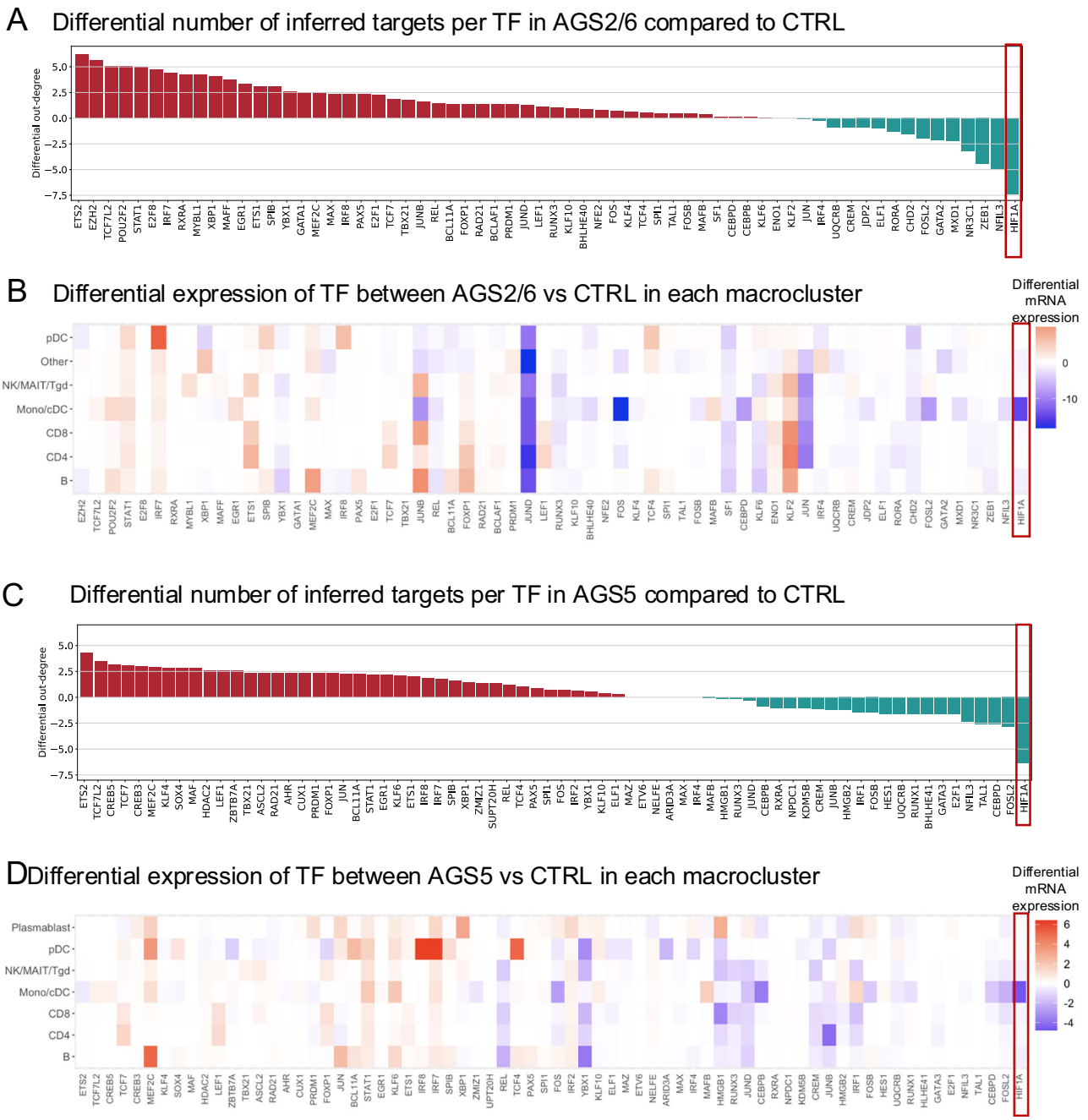

Fig. 2 | Predicted loss of HIF-1α activity in AGS patients, from gene regulatory network analyses. A Analysis of the differential number of inferred targets for each TF between AGS and CTRL calculated from the GRN from AGS2/AGS6/COPA integration. Top50 TF with highest number of predicted targets in CTRL are represented. Red bars highlight TF with increased score in AGS compared to CTRL while green bars highlight TF with decreased score in patients. Red square indicates the TF with the most important loss of predicted targets in AGS. **B** Heatmap of the differential mRNA expression between AGS and CTRL of each TF extracted from the GRN in each macrocluster of AGS2/AGS6/COPA integration. Differential expressions were calculated by subtracting the count of each TF in AGS group to the count in CTRL group. Red square highlight *HIF1A*. Color scale indicate differential expression of TF upregulated in AGS (red) and downregulated (blue). **C** Analysis of the differential number of inferred targets for each TF between AGS and CTRL calculated from the GRN from AGS5 integration. Top50 TF with highest number of predicted targets in CTRL are represented. Red bars highlight TF with increased score in AGS compared to CTRL, while green bars highlight TF with decreased score in patients. Red square indicate the TF with the most important loss of predicted targets in AGS. **D** Heatmap of the differential mRNA expression between AGS and CTRL of each TF extracted from the GRN in each macrocluster of AGS5 integration. Differential expressions were calculated by subtracting the count of each TF in AGS group to the count in CTRL group. Red square highlight *HIF1A*. Color scale indicate differential expression from expression of TF upregulated in AGS (red) and downregulated (blue).

with downregulation of glycolysis (Fig. 4E **right)** as in AGS patients' PBMC (Figs. 3A, B and S3A).

On day 6 after transduction with shRNA in the 3 AGS cellular models, Seahorse experiments confirmed lower glycolytic activity and reduced maximal glycolytic capacity (Figs. 4F, G, H, and S4G) indicative of metabolic reprograming in AGS models. The reduced glycolytic activity was associated with mitochondrial stress, as shown by the increased expression of stress related genes by qRT-PCR (*CLPP* and *HSP60*) (Fig. 4I) and increase in mitochondrial ROS detection by flow cytometry (Fig. 4J and S4H). Cytosolic double-strand DNA

https://doi.org/10.1038/s41467-026-69979-9

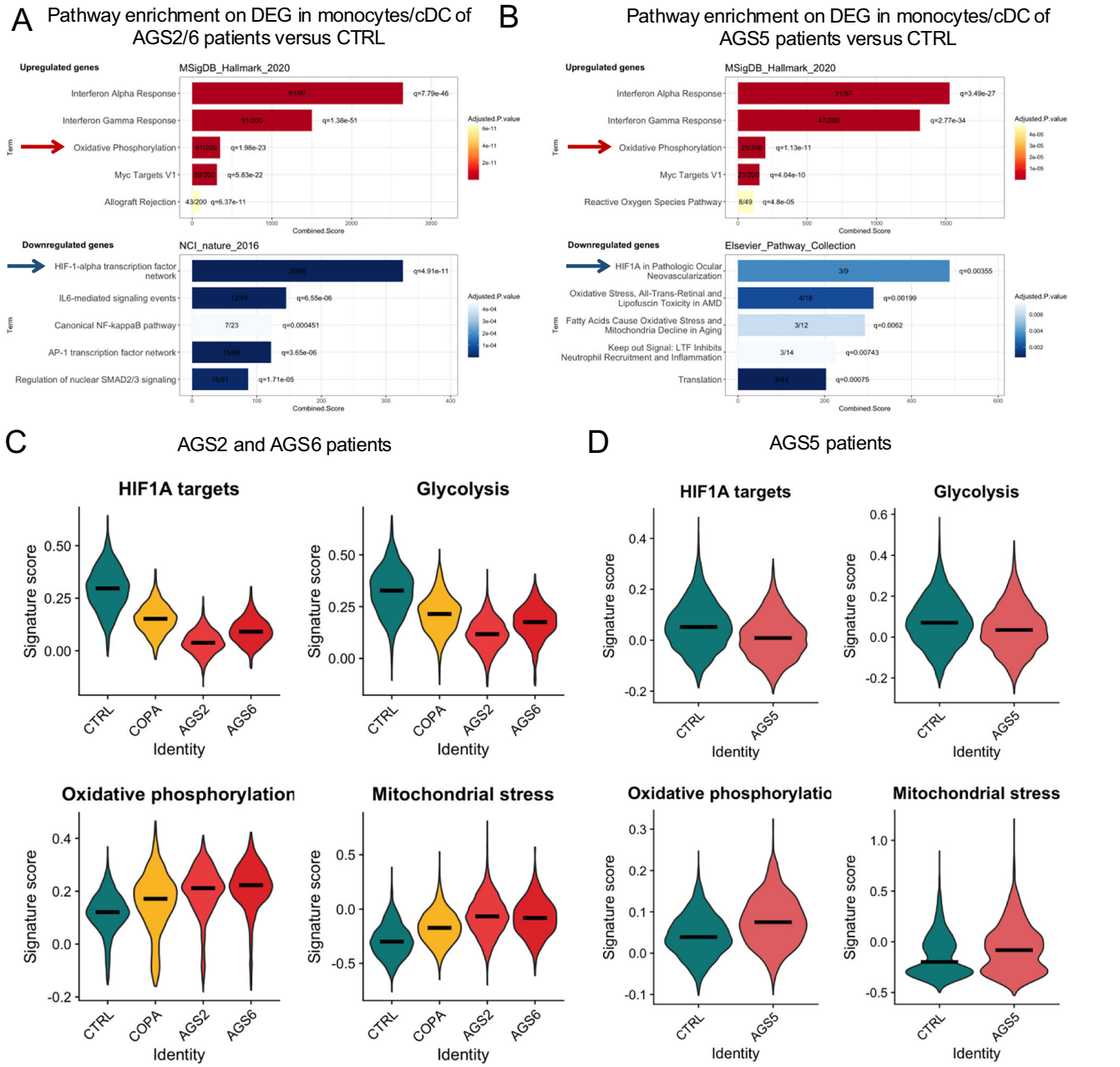

Fig. 3 | HIF-1α loss of activity and energy metabolism switch in monocytes/cDC of AGS patients. A, **B** Pathway enrichment analysis using EnrichR of differentially expressed genes (DEG) in AGS2/AGS6 patients (**A**), or AGS5 patients (**B**), compared to respective CTRL group. Pathways are ranked based on combined score. Color gradient is proportional to adjusted *p* value of one-sided Fisher's test. Numbers indicates the number of genes present in the DEG list over the total number of genes referenced in the corresponding pathway. Red color highlights pathways counting genes upregulated in patients and blue color highlights pathways counting downregulated genes in patients. Red arrows point toward Oxidative phosphorylation associated pathways and blue arrows point toward anaerobic glycolysis and HIF-1α-related pathways. **C**, **D** Violin plots of the signature score for "Oxidative phosphorylation pathway" (MSIgDB hallmark database), for "Glycolysis Activation in Cancer Warburg Effect" (Elsevier database), for HIF-1α known targets expression from NCI- Nature database ("HIF-1-alpha transcription factor network Homo sapiens") and for "Mitochondrial stress" (see gene lists in SI2) in monocytes/cDC split by groups of AGS2/AGS6/COPA integration (**C**) and AGS5 integration (**D**). Medians are shown as black lines.

(dsDNA) and RNA (dsRNA) measurements, in addition of TOMM40 staining were performed by confocal microscopy (figure S4J). Cytosolic events of dsDNA and dsRNA were identified in AGS cellular models. A high proportion of cells presented a 2-fold increase in cytosolic nucleic acid compared to scr in SAMHD1 knock-down model (41.2% with dsDNA and 23.5% with dsRNA), in ADAR knock-down model (15.8% with dsDNA and 30.1% with dsRNA) and in RNASEH2B model (31.6% of dsDNA and 26.2% of dsRNA) (figure S4J). A partial detection in accordance with the percentage of cells responding to type I IFN, with 10 to 50% of cells on average across the 3 AGS cellular models, expressing ISG15 (Fig. 4C).

To assess the involvement of type I IFN in metabolic reprogramming, type I IFN blocking antibodies were used on AGS cellular models. Alongside a shutdown of IFN response, shown by reduced levels of ISG15 expression and IP-10 production (Figs. 4K, L), glycolytic capacity was restored (figure S4I). A direct effect of IFN response on metabolic reprogramming, was also studied after in vitro stimulation of control MDDC with type I IFN. Besides the expected increase in ISG15

https://doi.org/10.1038/s41467-026-69979-9

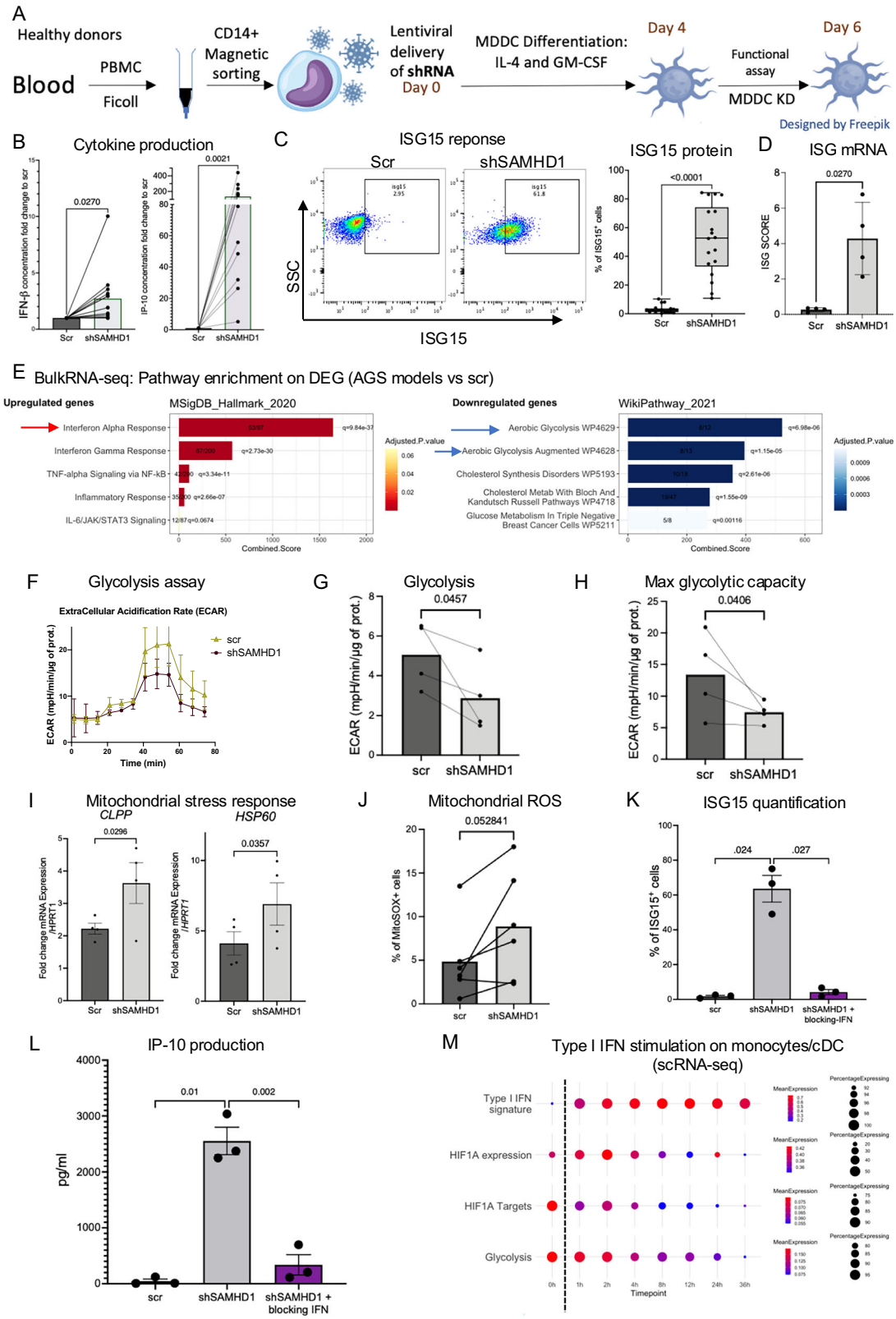

expression upon MDDC stimulation with type I IFN (figure S4K), a 3-fold decrease in glycolytic activity and maximal glycolytic capacity was observed by seahorse assay (figure S4L). In addition, in cells stimulated by recombinant type I IFN and assessed by scRNA-seq at different time points[16] (Fig. 4M and S4M), a time dependent increase in type I IFN response was associated with a decrease of both HIF-1α targets and glycolysis associated gene expressions, specifically in monocytes/cDC subtype (Fig. 4N). While *HIF1A* expression was increased at early time points, a gradual decrease in HIF1A expression from 2 h to 36 h following IFN stimulation, was observed (Fig. 4N). These results are in accordance with other studies reporting that type I IFN affects energy metabolism[32–34].

Fig. 4 | Confirmed metabolic switch, mitochondrial stress and type I interferon response on in vitro models of AGS. A Protocol for shRNA transduction of MDDC. **B** Cytokine measurement in supernatant of MDDC at day 6 post transduction ($n = 13$). **C** Representative flow plots of ISG15 signal in MDDC at day 6 post transduction (left). Quantification of the percentage of ISG15 positive cells ($n = 18$) (right). Box-and-whisker plots show the median, the 25th–75th percentiles and the full data range. **D** ISG score based on mRNA quantification in MDDC (*ISG15, IFI44L, IFIT1, IFI27, RSAD2* and *SIGLEC1*) at day 5 after transduction ($n = 4$). **E** Bulk RNA seq on MDDC from two blood donors transduced with shADAR, shSAMHD1 or shRNASEH2B for 6 days (AGS models) or control (scr). Pathway enrichment analysis in AGS cellular models is shown. Pathways are ranked based on combined score. Color gradient is proportional to adjusted p value of a one-sided Fisher's test. **F** Representative time course of extracellular acidification rate (ECAR) from MDDC at day 6 after transduction. Mean with standard deviation of 3 replicates from 1 representative donor. **G**, **H** Quantification of extracellular acidification rate (ECAR) presented in Fig. 4F due to maximal glycolytic capacity (**G**) or actual glycolysis (**H**) ($n = 4$). ECAR was measured and normalized to the quantity of protein in each well. **I** *CLPP* and *HSP60* genes mRNA level, from MDDC at day 5 after transduction normalized to *HPRT1* mRNA level ($n = 4$). **J** Flow cytometry quantification of mitochondrial ROS production at day 6 after transduction ($n = 6$). **K**, **L** At day 4 after transduction, a type I IFN blocking antibodies cocktail (1/200 dilution factor) was added to MDDC knock-down for SAMHD1 for 48 h. Flow cytometry of ISG15 (**K**) and quantification of IP-10 production by legendplex (**L**) are shown. One-way anova statistical test results are presented with SEM ($n = 3$). **M** PBMC from healthy donors stimulated with type I IFN in vitro were analyzed by scRNA-seq at different timepoints. Markers and signatures level are shown as dot plot. **B**–**D**, **G**–**J** Mean and SEM are represented with two-tailed paired t-test statistics. scr: MDDC transduced with a control shRNA; shSAMHD1: SAMHD1 targeting shRNA.

Stabilization of HIF-1α reverted the energy metabolism switch, relieved mitochondrial stress and inhibited type I IFN response in AGS cellular models

To investigate whether the lack of HIF-1α activity and the energy metabolic switch observed in AGS MDDC models could be reverted, the prolyl hydroxylase inhibitor dimethyloxalylglycine (DMOG), known to prevent HIF-1α degradation, was used[35,36] (figure S5A). Addition of 500 μM of DMOG increased HIF-1α protein levels as early as 5 h post incubation (Fig. 5A). First, the impact of DMOG treatment was evaluated at the transcriptomic level using the bulk-RNAseq data generated on treated MDDC models of AGS (figure S5B). DEG between AGS cellular models (*SAMHD1*, *ADAR1* and *RNASEH2B*) treated with DMOG against untreated cells followed by pathway enrichment analysis showed a rescue of glycolytic genes expression and HIF-1α transcriptional program associated with reduced inflammatory response upon treatment (figure S5C). An observation confirmed by directly plotting the mean expression of HIF-1α targets and glycolysis genes used in scRNA-seq of AGS patients' PBMC (figure S5D and S5E). Functional assays also revealed that HIF-1α stabilization reduced both maximal respiratory capacity and ATP synthase activity (oxidative phosphorylation), while increasing anaerobic glycolysis activity and maximal glycolysis activity (Fig. 5B and S6A–S6D). Taken together, these results suggest that glucose consumption was redirected from mitochondrial respiration toward anaerobic glycolysis, thereby correcting the metabolic switch observed in AGS models. Consistent with reduced mitochondrial activity, following DMOG treatment, *CLPP* and *Hsp60* gene expression were reduced (Fig. 5C). Finally, stabilizing HIF-1α upon DMOG treatment, effectively reduced the type I IFN response in AGS cellular models at the mRNA (Fig. 5D) and protein level for ISG15 and IP-10 (Figs. 5E, F, S6E and S6F)).

To assess the significance of HIF-1α-mediated regulation of mitochondrial activity, rotenone was used as a direct disruptor of mitochondrial electron transport chain in AGS cellular models to induce a shutdown of mitochondrial respiration. Mitochondrial respiration was reduced by two-fold in AGS cellular models (Fig. 5G and S6G) and compensated by an increase in glycolytic capacity (Fig. 5G and S6H). Consequently, type I IFN response measured by ISG15 expression and IP-10 production was reduced (Fig. 5H, S6I and S6J) supporting involvement of effective oxidative phosphorylation on the type I IFN response in AGS cellular models.

Targeted metabolite measurement confirmed energy metabolic switch in AGS patients reverted following DMOG addition in AGS cellular models

To confirm metabolic imbalance in AGS patients, metabolite measurement was performed in PBMC of some of the samples previously used for scRNA-seq (P1 to P4), hence including AGS2 and AGS6 patients, and controls (see supplementary data 1**)**. Relative metabolite levels were measured between AGS2, AGS6 and controls samples (figure S7A). Dendrogram repartition of samples revealed a clear distinction between controls and patients' samples based on metabolite profiles, while AGS2 and AGS6 samples were more similar to each other (figure S7B). AGS patients' samples clustered together in the PCA (Figs. 6A and 6B) and are associated with metabolites involved in ROS response such as glutathione metabolism (GSH/GSSG) and precursors of TCA cycle intermediate like glutamate (GLU) /glutamine (GLN) or succinic acid (Figs. 6C, 6D **and** S7C). Opposingly, control samples are associated with glycolytic intermediates (PEP, G6P, DHAP) or related pathway (glycerol-3-phosphate and pentose phosphate pathway (PPP)). Numerous amino acids were also found accumulating in controls indicative of an anabolic energy metabolism while patients' cells relied more on catabolic metabolism, coherent with increased mitochondrial activity (Fig. 6C).

Relative quantification of metabolites was then performed on AGS cellular models in presence or not of DMOG (figure S7D) to assess HIF-1α stabilization on metabolite accumulation. Sample repartition by PCA (Fig. 6E) and dendrogram (figure S7E) revealed a distinction of metabolic profiles between control cells (scr) and AGS MDDC models (shSAMHD1, shADAR, shRNASEH2B) and, more strikingly, between DMOG treated and untreated cells thereby suggesting a deep remodeling of metabolic pathways in these conditions. PC1, from PCA analysis, illustrated differences between DMOG treated cells and untreated cells (Fig. 6F **left panel**) while PC2 better represented differentially quantified metabolites between control cells (scr) and MDDC models of AGS (Fig. 6F **right panel**). AGS cellular models were associated with accumulation of glutathione (GSH), a ROS scavenger indicative of oxidative stress[37], and TCA feeding metabolite glutamate (GLU) (figure S7F **right panel**). Control cells clustering was driven by accumulation of glycolytic intermediates (lactate, pyruvate, glyceraldehyde-3-phosphate) or related pathway like pentose phosphate pathway (Sedoheptulose-7-phosphate) (figure S7F **right panel**). Thus, in vitro metabolite measurements in AGS cellular models are comparable with results in AGS patients' PBMC. Importantly, stabilizing HIF-1α protein expression with DMOG dampened the excess of mitochondrial respiration and redirected energy production towards glycolysis (Fig. 6G). DMOG treated cells were associated with increased amino acid metabolism, glycolysis (PEP), pentose phosphate pathway (ribose-5-phosphate) and a decrease in TCA intermediates (malate, fumarate) (Figs. 6G, H **and** S7F **left panel**). Glycolytic intermediates G3P, pyruvate and lactate, that were found downregulated in AGS cellular models, were particularly increased in DMOG treated cells (Fig. 6H). DMOG treatment also reduced GSSG level, that was found elevated in AGS cellular models and AGS patients' cells suggesting a relieved oxidative stress (Fig. 6H). HIF-1α stabilization with DMOG allowed cells to enter an anabolic state using glycolysis for energy production while untreated AGS cellular models and AGS patients

https://doi.org/10.1038/s41467-026-69979-9

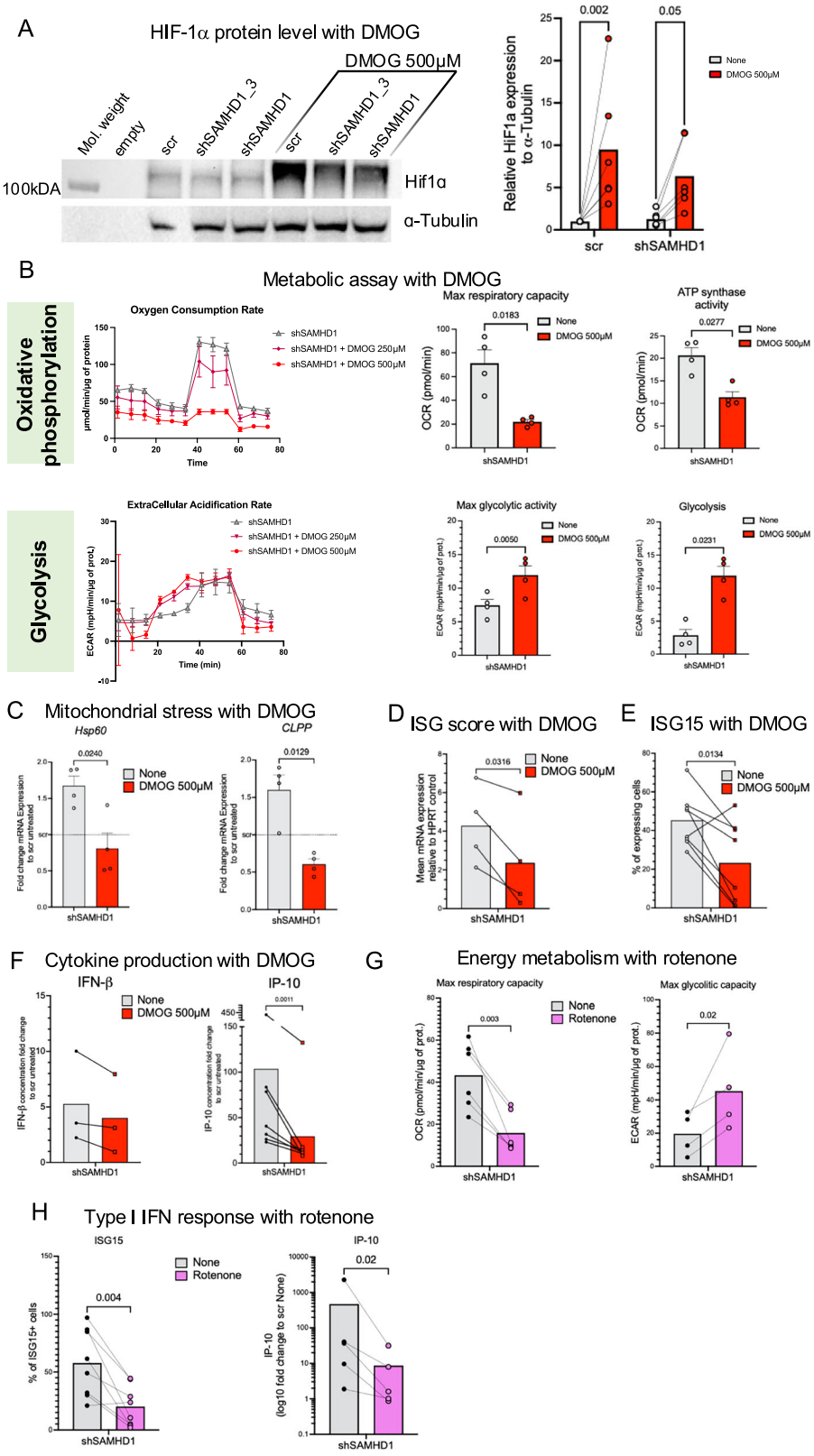

'cells appeared to be in a catalytic state with low glycolytic activity (Fig. 6G).

In conclusion, the metabolic imbalance of AGS patient cells, first suggested at the transcriptomic level, was confirmed at the metabolite level, with reduced glycolytic activity and anabolic state in favor of high mitochondrial activity and catabolic state. Moreover, elevated glutathione metabolism in patient cells can be related to ROS accumulation. HIF-1α stabilization by DMOG reverted these metabolic changes in in vitro AGS cellular models.

Discussion

Molecular model for AGS pathogenesis

Our observations on molecular events contributing to AGS pathogenesis in PBMC, drawn from scRNA-seq analysis and in vitro

Fig. 5 | Stabilization of HIF-1α at the protein level, reversed energy metabolism switch, released mitochondrial stress and suppressed type I IFN response in SAMHD1 deficient cells. At day 4 after transduction, MDDC transduced with shRNA targeting *SAMHD1* were treated with the HIF-1α stabilizing drug dimethyloxalylglycine (DMOG) or rotenone (1 μM). **A** HIF-1α level of protein expression is represented compared to α-tubulin (**left panel**) with quantification on multiple donors ($n = 6$) (**right panel**) after 24 h of DMOG. Two different shRNA targeting SAMHD1 (shSAMHD1_3 and shSAMHD1) were used. Mean and *p* value of a paired two-way anova test are represented. **B** Time course of oxygen consumption rate (OCR) (**top panels**) and extracellular acidification rate (ECAR) (**bottom panels**). A representative time course is represented for 1 donor showing mean measurement with standard error of triplicates. Bar plots show quantifications on 4 donors relatively to the total of protein after 48 h of DMOG. **C** *CLPP* and *Hsp60* mRNA level after 24 h of DMOG normalized to *HPRT1* expression ($n = 4$). Data are presented as fold change to scr condition. **D** ISG score based on mRNA quantification (*ISG15, IFI44L, IFIT1, IFI27, RSAD2* and *SIGLEC1*) on MDDC after 24 h of DMOG ($n = 4$). **E** Quantification of the percentage of ISG15 positive cells in flow cytometry among MDDC after 48 h of DMOG ($n = 8$). **F** Cytokine measurement MDDC supernatant after 48 h of DMOG for IFN-β ($n = 3$) (**left**) and IP-10 ($n = 7$) (**right**). Only donors with detectable level of cytokine were kept. Data are presented as fold change to scr condition. **G** Maximal respiratory capacity (**left panel**) and maximal glycolytic capacity (**right panel**) were quantified after 48 h of rotenone. **H** Quantification of the percentage of ISG15 positive cells by flow cytometry (**left panel**) and IP-10 production in the supernatant by legendplex (**right panel**) among MDDC after 48 h of rotenone. (**B**–**H**) On bar graphs, means ± SEM and two-tailed paired T test statistics are represented. Each point represents a donor.

validation by functional assays, are summarized in the following model, in accordance with existing literature (Figs. 7A–C). Oxidative phosphorylation is the favored pathway to generate energy from glucose, but is a source of reactive oxygen species (ROS), a known inducer of oxidative stress[38]. In healthy individuals, HIF-1α, a sensor of oxidative stress[23], regulates ROS production by favoring glucose processing through anaerobic glycolysis, bypassing oxidative phosphorylation (Fig. 7A)[24]. The switch of energy production from oxidative phosphorylation toward anaerobic glycolysis is called the Warburg effect, first described in cancer cells[39]. Later studies have established the importance of this energy metabolic switch in critical cellular processes such as immune cell proliferation[40] or stem cell activation[41].

In AGS patients' monocytes/cDC, HIF-1α activity is suppressed (Fig. 7B). Thus, mitochondrial ROS can accumulate, increasing oxidative stress and chronic mitochondrial stress[38]. This mechanism is expected to be even more important in cells with high ROS content such as myeloid cells. Mitochondrial stress results in the release of mtDNA/mtRNA and in imbalance of metabolite, with reduced glycolytic intermediates and increased oxidized glutathione. This work suggests that cells favor a catabolic state to fuel excessive oxidative phosphorylation activity and that mitochondrial activity participates to increase type I IFN response in AGS (Fig. 7B).

In an in vitro cellular model of AGS, HIF-1α stabilization by the synthetic chemical compound DMOG, allowed a switch of energy metabolism toward anaerobic glycolysis, even in the presence of type I IFN. Consequently, mitochondrial stress is relieved and the ISG response including IP-10 production is reduced, breaking the cycle of type I IFN response (Fig. 7C).

HIF-1α activity under type I IFN signaling in monocytes/cDC

scRNA-seq data in AGS patients suggest a close relationship between an elevated type I IFN response and low levels of *HIF1A* expression. To our knowledge, only one study reported a potential link between type I IFN and HIF-1α, showing ISG15 capacity to reduce HIF-1α protein levels through proteasome induced degradation without affecting mRNA levels[42]. While ISG15 likely plays a role, we do not exclude a potential role of other ISG in the regulation of *HIF1A*. Moreover, our data highlight an inhibition of *HIF1A* transcription associated with a deep reprogramming of energy metabolism. Finally, a type I IFN response has been shown to induce genes involved in oxidative phosphorylation over anaerobic glycolysis in human monocyte-derived cells ([43] and the present study), coherent with a reduced *HIF1A* activity.

Uncontrolled oxidative phosphorylation induces mitochondrial stress

Our data suggest that lack of *HIF1A* expression prevents AGS monocytes/cDC from regulating oxidative phosphorylation by switching to anaerobic glycolysis. We hypothesize that overactivation of oxidative phosphorylation, both in intensity and in time, favors mitochondrial stress in AGS. One good candidate for oxidative phosphorylation induction of mitochondrial stress is ROS generation by electron transport chain complexes[38], found elevated in AGS cellular models (Fig. 5K and S5H). Two independent teams recently performed genome wide association studies (GWAS) on large cohorts to identify single nucleotide polymorphisms (SNP) associated with a disturbance of mitochondrial mtDNA copy number[44,45]. Both studies revealed that SNP in *SAMHD1* correlates with an increase in mtDNA copy number (indicative of oxidative stress in the mitochondria[46,47]). Moreover, metabolite measurement revealed increased level of oxidized glutathione in AGS patients (Fig. 6D), another indication of oxidative stress[37,48,49]. We also noted that AGS has been suggested to involve a disturbance of mitochondrial activity in some patients[50,51]. Notably, a recent report revealed alteration of mitochondrial integrity associated with uncontrolled oxidative phosphorylation, increased ROS activity and mitochondrial stress in AGS patients mutated in *RNASEH2A* or *RNASEH2B*[52]. We propose here that loss of HIF-1α activity could be a driver of mitochondrial dysfunction in AGS. Accordingly, when HIF-1α was stabilized in our in vitro cellular models oxidative phosphorylation was reduced, and mitochondrial stress relieved (Fig. 5 and S6).

Tight interplay between energy metabolism and the type I IFN response

We provide evidences that mitochondrial activity is involved in the type I IFN response in AGS (Fig. 5 and S6). Chronic mitochondrial stress can drives a loss of mitochondrial membrane integrity and the release of double strand mtDNA and mtRNA into the cytoplasm[38]. dsDNA and dsRNA structures in the cytosol observed in AGS cellular model in vitro (figure S5J) have been previously reported to induce type I IFN production by activating nucleic acid pathways through MDA5 and STING[38,53,54].

In addition to nucleic acid, this study highlights imbalance in metabolites, particularly through an increase in glutamine derivates (glutamine and oxidized glutathione) associated with a decrease of glycolytic/pentose phosphate intermediates (glucose-6-phosphate and ribose-6-phosphate) in AGS patients. Others have shown in murine models that accumulation of metabolites such as fumarate[55] or itaconate[56] can trigger type I IFN responses by favoring mtDNA/dsRNA release, but level of these particular metabolites remained not significantly changed in our study. Additionally, depletion in some metabolite can also favor type I IFN production. For example, lactate, the end product of anaerobic glycolysis is a potent inhibitor of MAVS activation, effectively dampening type I IFN induction in a mouse model[57]. Interestingly, inhibition of type I IFN response by HIF-1α stabilization in vitro was associated with elevated lactate levels and reduced levels of glutamine derivates, glutamate and glutathione (Figs. 6G and 6H) that was particularly elevated in AGS patients (Fig. 6D). Our work unveils a role of mitochondrial activity on type I IFN response in AGS but the exact trigger remains elusive. dsRNA/DNA release and metabolite imbalance have been identified as potential inducers of type I IFN[55,56], however the nature of nucleic structures and the type of metabolite accumulating might differ between the different gene mutated in AGS. For example, more than 30% of cell in AGS

https://doi.org/10.1038/s41467-026-69979-9

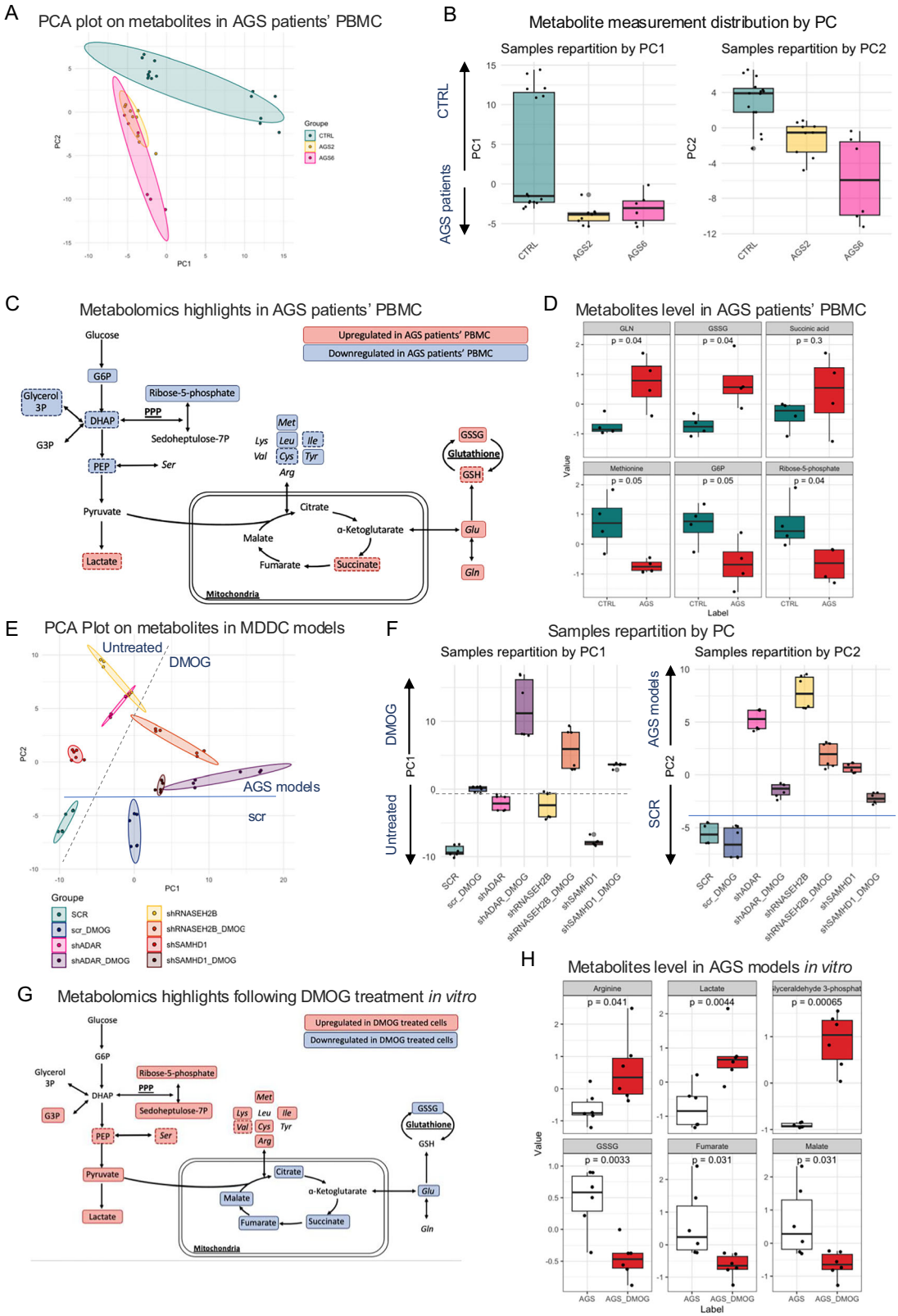

cellular models of ADAR mutation are accumulating dsRNA but less than 16% showed accumulation of dsDNA structures in the cytosol, coherent with its role of RNA editing (figure S5J). Additionally, researchers have recently described a monocytic cell line knockout for SAMHD1 presenting spontaneous type I IFN response associated with mitochondrial DNA sensing[58]. More studies are therefore required to better understand the relative contribution of metabolite imbalance and/or the mtDNA/mtRNA sensing responsible of type I IFN in each genotype of AGS.

Within the type I IFN response, IP-10 production was particularly increased in AGS cellular models (Fig. 5B and S5E) and was drastically inhibited upon HIF-1α stabilization (Fig. 5F and S6F). IP-10 is one of the most highly expressed inflammatory cytokines produced in response to type I IFN and is detected in plasma and cerebrospinal fluid (CSF) of

Fig. 6 | Metabolomic analyses and energy metabolism imbalance in AGS, reverted by DMOG treatment. Related to Fig. 6. A–D Targeted metabolite measurement by LC/MS on PBMC of AGS patients with ADAR mutation (AGS6, $n = 2$), RNASEH2B mutation (AGS2, $n = 2$) and healthy donors (CTRL, $n = 4$). **A**, **B** Principal component analysis (PCA) on metabolite quantification in patients and controls (**A**) with sample repartition among PC1 and PC2 (**B**). Technical triplicates for each sample are shown. **C** Highlights of cellular energy metabolism in AGS patients. Metabolites found upregulated or downregulated in AGS patients' cells are respectively highlighted in red or blue. Metabolites with doted outlines stood out from PCA but did not reach two-tailed t-test significance ($p < 0.05$). **D** Box plots of metabolite relative levels. Mean level in each individual is represented as a dot. *P* values of a paired two-tailed statistical t-test are indicated. **E–H** MDDC from two healthy donors were transduced with shRNA targeting ADAR, SAMHD1 or RNASEH2B mRNA for 4 days, then treated or not with DMOG before metabolite measurement at day 6 by LC/MS. Cells in SCR condition are transduced with a control shRNA. **E**, **F** Principal component analysis (PCA) on metabolite quantification in MDDC models (**E**) with sample repartition among PC1 and PC2 represented as a box plot (**F**). Cutoffs have been drawn to show separation between scr condition and AGS models (blue line) and between DMOG treated cells and untreated cells (dashed line). Technical triplicates for each sample are shown. **G** Highlights of cellular energy metabolism in DMOG treated AGS in vitro models. Metabolites found upregulated or downregulated in DMOG treated cells are respectively highlighted in red and blue. Metabolites with doted outlines stood out from PCA but did not reach two-tailed t-test significance ($p < 0.05$). **H** Box plots of metabolite relative levels. Mean level in each individual is represented as a dot. *P* values of a statistical two-tailed t-test are indicated. **B**, **D**, **F** and **H** Box-and-whisker plots show the median, the 25th–75th percentile and the full data range.

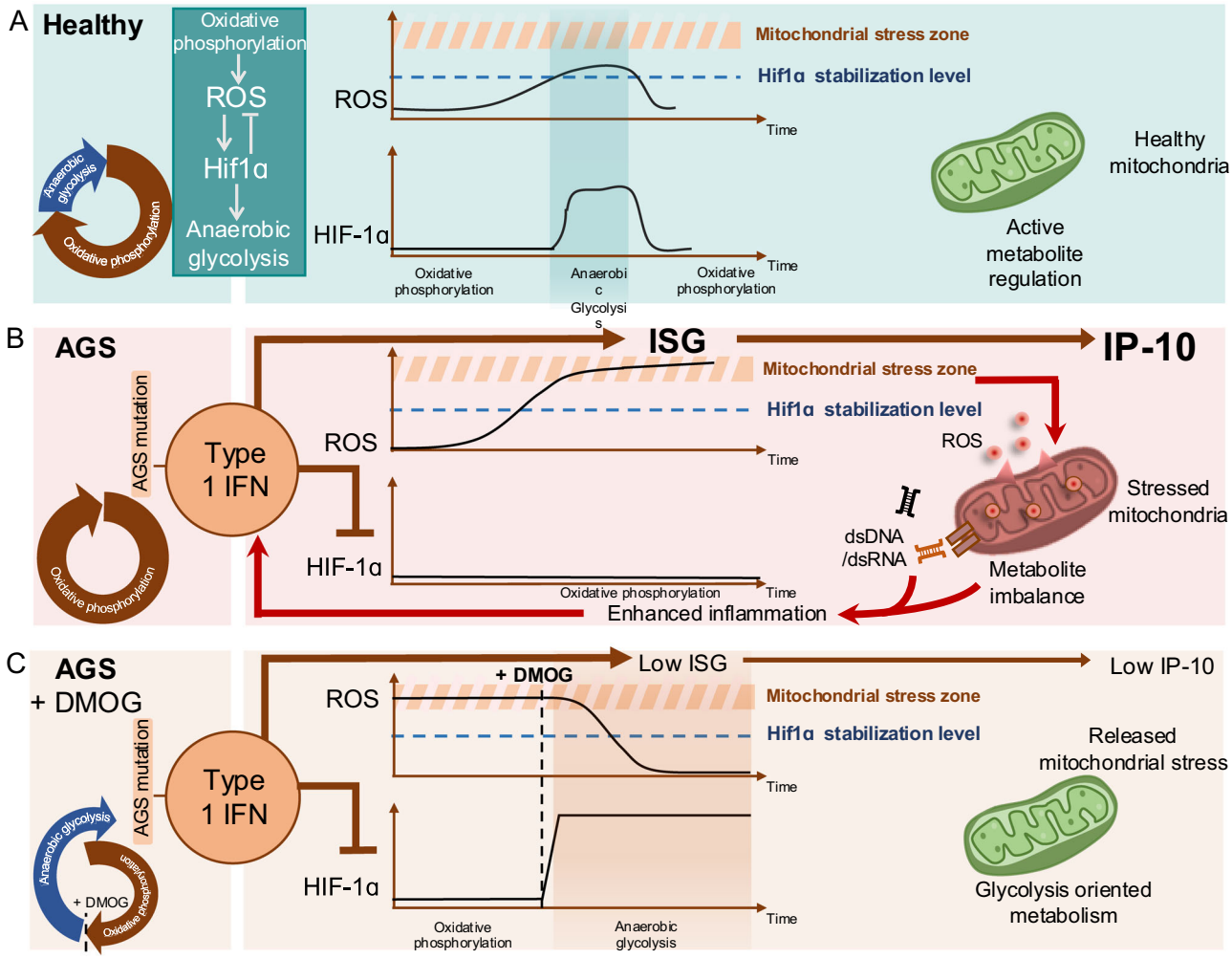

Fig. 7 | Graphical representation of energy metabolism regulation of type I IFN response through HIF-1α. A–C Model combining data presented in this manuscript and current literature. **A** HIF-1α is known to sense and control ROS production through oxidative phosphorylation pathway, by balancing energy metabolism toward anaerobic glycolysis. **B** In AGS patients, a loss of HIF-1α activity and expression were observed and associated with an energy metabolism locked in oxidative phosphorylation state, aggravated mitochondrial stress and excessive IP-10 production. In this context, HIF-1α stabilization prevented type I IFN response (ISG expression) and notably shut down of IP-10 production. Accordingly, without HIF-1α, uncontrolled ROS production and excessive oxidative phosphorylation might participate to elevated IFN response and IP-10 production in AGS patients. **C** In vitro treatment using DMOG on MDDC models of AGS, restored HIF-1α activity, reverted energy metabolism, released mitochondrial stress and reduced type I IFN response (ISG expression) and notably shut down of IP-10 production. ROS= Reactive oxygen species; HIF-1α= Hypoxia inducible factor 1α; AGS= Aicardi Goutières syndrome; IP-10= Interferon inducible protein 10; dsDNA/dsRNA= double stranded (deoxy)ribonucleic acids; DMOG= dimethyloxalylglycine.

AGS patients[10]. Its proinflammatory role has been attributed to an induction of chemotaxis of inflammatory cells such as monocytes, NK cells, activated T cells and neutrophils[59]. IP-10 can also negatively regulate angiogenesis[60] and possess neurotoxic capacity[11] which could relate to respectively the high frequency of vasculitic chilblain-like lesions and deleterious neurological manifestations in AGS. We show that, among PBMC, cells with the highest type I IFN response at the mRNA level are monocytes/cDC. Moreover, in vitro MDDC models of AGS produced high levels of IP-10, arguing for an important role for monocytes/cDC in the production of IP-10 in AGS patients.

While a switch of energy metabolism in presence of type I IFN has previously been observed in different contexts[32–34,43], our in vitro experiments using HIF-1α stabilizing drugs and mitochondrial respiration inhibitor showed that targeting energy metabolism can effectively impact type I IFN response, encouraging the development of future clinical assays modulating energy metabolism in AGS and type I interferonopathies in general. Notably, HIF-1α stabilizing drugs have already gone through all clinical phases for their safety and efficiency in the context of anemia[61,62]. Effective dampening of IFN response have also been observed when mitochondrial activity was perturbated in other contexts[55,63].

Regulation of HIF-1α or targeting energy metabolism pathways might thus be a promising therapeutic approach in conditions involving excessive type I IFN signaling, such as AGS but also polyfactorial disorders such as systemic lupus erythematous.

Limitations of the study

The main limitation in the use of scRNA-seq techniques is gene dropout, as it is estimated that only the most expressed genes are detected (around top 15-20% in each cell, depending on the cell type). Thus, the role of lowly expressed genes is overlooked. Nevertheless, scRNAseq allowed us to explore all populations of immune cells and to highlight a previously unknown importance of monocytes/cDC in the pathology. In addition, we were able to draw similar conclusions on AGS patients despite exploring independent experiments and integrations of scRNA-seq data from patients with different mutations, reinforcing our conclusions on AGS pathogenesis. Another limitation of scRNA-seq is that molecular changes observed at mRNA level does not necessary translate into functional molecular changes at the protein level. However, scRNA-seq data were used to generate hypothesizes that were then validated functionally on three different in vitro models and confirmed by metabolite measurement using LC/MS on AGS patients' PBMC.

AGS is a rare genetic disorder, so we present here a study on a total of 6 patients of 3 different genotypes. In this study, the limited number of samples can limit generalization of data interpretation. Nevertheless, potential discrepancies are addressed through a combination of supervised (classical DEG) with unsupervised (GRN) approaches for scRNA-seq analysis and the development of three in vitro models of *SAMHD1, ADAR* and *RNASH2B* deficient primary cells.

Finally, in this study, the focus was on circulating immune cells, in monocytes/cDC in particular, our area of expertise, but we do not exclude that energy metabolism imbalance could be relevant in other immune cells such as macrophages and plasmacytoid DC[64] and/or have disruptive effects in non-circulating cell types, such as neurons or glial cells during brain development in AGS patients.

Methods

Lead contact

Further information and requests for resources and reagents should be directed to and will be fulfilled by Mickaël Ménager (mickael.menager@institutimagine.org).

Experimental model and subject details

Patients. Patients were aged between 3 and 16 years old with the exception of P6 being 36 years old and were included based on molecular diagnosis of biallelic loss of function mutations in *SAMHD1*, *RNASEH2B* or *ADAR1* genes for AGS or dominant-negative mutation in *COPA* gene for patients with COPA disease. COPA syndrome is a type I IFN-driven disease mediated through chronic STING activation even in the absence of aberrant nucleic acid sensing[15]. However, in contrast to AGS, COPA patients suffer from systemic inflammation including chronic lung inflammation in the absence of overt neurological involvement. P1, P2, P7 and P8 studied in this work have been previously reported by Rice at al. respectively labeled P0002, P0004, P0003 and P0011[65]. PBMC were frozen the day of sampling and thawed once for scRNA-seq library generation. P1 was undergoing RTI tri-therapy (zidovudine, abacavir, lamivudine) for 5 months. PBMC from P8 were extracted before and after 1 month of RTI tri-therapy (zidovudine, abacavir, lamivudine). Other patients and healthy donors were not under therapy. The study was approved by the *Comité de protection des personnes Iles de France II* and the French advisory committee on data processing in medical research (ID-RCB: 2014-A01017-40). Consent of parents and/or patients, depending on age, was obtained for conducting the experiment. 7 control samples were assessed using PBMC from anonymous healthy individuals aged between 22 to 32 years old of both genders after voluntary blood donation at *Etablissement Français de Sang*.

Cells. To generate monocytes derived dendritic cells (MDDCs) form human primary cells, we acquired buffy coats from healthy human donors (*Etablissement Français de Sang*). We performed Ficoll extraction of peripheral blood mononuclear cells (PBMC) and used anti-human CD14 magnetic beads (Miltenyi) to purify monocytes. Magnetic sorting was performed on AutoMACS pro separator device (Miltenyi Biotech). Isolated monocytes were cultured in RPMI (Gibco), 10% FBS (heat inactivated, Sigma), 10 mM Hepes, 55 μM β-mercaptoethanol, 6 mM L-glutamine, 50 μg/ml Gentamicin and 100 U/ml Penicilin/Streptomycin (Gibco) in the presence of 10 ng/mL of human recombinant GM-CSF and 50 ng/mL of human recombinant IL-4 (Miltenyi) to induce MDDC differentiation[66]. Multiple lot of FBS were tested and selected according minimal induction of CD86 expression on MDDC. 5×10^6 cells/mL of $CD14^+$ cells were plated in 10 cm culture plates (Sigma) and cultured for 4 days before functional assays to allow complete MDDC differentiation, which was assessed by flow cytometry following CD14 loss of expression and DC-SIGN upregulation. Fresh media with cytokines (20% of total volume) was added at day 1 and day 3. At day 4 of cultures, cells were washed with fresh medium, counted and plated on 96 wells culture plates (Falcon) for stimulation and functional assays at the indicated times.

PBMC collected from patients were isolated by Ficoll-Paque density gradient (Lymphoprep, Proteogenix) from blood samples using standard procedures. PBMC were frozen in liquid nitrogen in DMSO 10% FBS 90%. scRNA-seq experiment were performed immediately after thawing.

Method details

Plasmids and viral particle production. *SAMHD1, ADAR and RNASEH2B* shRNA coding plasmids were purchased from SIGMA company and are detailed in key resources table. Vpx coding plasmid was used to allow monocytes transduction[67]. pLK0.1-GFP was used to assess transduction efficiency while pCMV- ΔR8.91 and pCMV-VSVg were used for packaging and pseudotyping of viral particles[68]. Plasmid amplification was achieved by transformation of Stblt3 bacteria (ThermoFisher) and ampicillin selection. All plasmids were then purified using Purelink Hipure plasmid midiprep kit (ThermoFisher). To produce VLP, coding plasmids were transfected into HEK293FT[69]: HEK293FT cells (R70007 Thermofisher Scientific) were cultured in DMEM (Gibco), 10% fetal bovine serum (FBS, heat inactivated) (Sigma), 0.1 mM MEM non-essential Amino Acids, 6 mM L-glutamine, 1 mM MEM sodium pyruvate, and antibiotics (Gibco). For generation of VLP containing plasmid of interest (scramble, GFP or shRNA), the day before transfection, cells were seeded on 10 cm culture plates to reach 70% confluence for transfection. To produce transfection reagent, 9,6 μg of plasmid of interest was prepared together with 6 μg Δ8.91 plasmid and 2,4 μg pCMV-VSV-g plasmid in DMEM complemented with 1/25 TransIT-293 transfection reagent (Mirus-Euromedex). The transfection reagent was then added drop by drop to HEK293FT. For generation of VLP containing Vpx (VLP/Vpx), HEK293FT were transfected by calcium-phosphate. The day before transfection, cells were seeded

on 15 cm culture plates to reach 70% confluence for transfection. Transfection reagent was composed of 50 μg pSIV3+ (Vpx coding plasmid[70]) with 10 μg pCMV-VSV-g plasmid in H_20 + 0,25 M $CaCl_2$ buffered by HBS according ProFection Mammalian Transfection protocol (Promega). Transfection reagent for VLP/Vpx was added drop by drop to HEK293FT. After one day, media of all transfected HEK293T cells (both for Vpx or plasmid of interest) was replaced with fresh medium. At day 2, supernatant was harvested and filtered twice using 0.45 μm sterile filters (Sigma). VLP were immediately used for monocytes transduction.

Lentiviral transduction. Monocytes were transduced immediately after magnetic sorting. Medium was complemented with 8 μg/ml polybrene (Sigma) to facilitate transduction, and cells were plated in 10 cm culture plates. 5×10^6 cells/mL of $CD14^+$ in 5 ml of complemented medium were transduced with 2,5 mL of VLP/Vpx and 4 mL of VLP containing plasmid coding shRNA, scramble or GFP[67]. Scramble transduced MDDC present unaffected transcriptomic profile and served as a point of reference for analysis. GFP coding plasmid allowed an assessment of transduction efficiency by flow cytometry. MDDC transduction efficiency > 90% at day 6 was considered satisfactory. Following shRNA were purchased from MeRk-Sigma companie: shSAMHD1 (Ref#3025348290 TRCN0000144540), shSAMHD1#3 (Ref#3025348290 TRCN0000141398), shADAR (Ref#3025348290 TRCN0000050792), shRNASEH2B (Ref#3025348290 TRCN0000 129159)

Cell culture. Cellular models of AGS were generated by lentiviral transduction of monocytes at day 0 and assessed at day 4 to reach optimal differentiation in MDDC and gene knock down by shRNA. Cells were then incubated with different drugs such as 500 μM of DMOG (Sigma D3695), 1 μM rotenone (R&D system 3616), 20 μM of recombinant IFNα2 (Biolegend 592704) or a 1/200 dilution of anti-IFN blocking antibody cocktail (Tebu-bio 39000-1) for 48 h to be assessed at day 6 post transduction. For mitochondrial ROS detection, cells were washed with warm PBS at day 6 and incubated with 1 μM of MitosSOX-Red probe (Thermo Fischer M36008) in warm PBS for 30 min at 37 °C 5% CO_2. Cells were washed 3 times with PBS before detection of MitoSOX staining by flow cytometry.

Flow cytometry analysis. For flow cytometry analysis, MDDCs were washed with PBS and first stained with LIVE/DEAD Fixable dye (ThermoFisher) in PBS for 15 min at 4 °C in the dark. After washing in PBS, cells were stained with antibodies for extracellular labeling for 25 min at 4 °C in PBS 1% Bovine Serum Albumin (BSA, Roche) and 1 mM EDTA (Life technology). For intracellular staining (ISG15), cells were fixed with cytofix/cytoperm (BD) for 15 min at room temperature then stained with antibodies in permeabilization buffer for 45 min at 4 °C. The following antibodies were used: PE-anti-human ISG15 (Bio-Techne IC8044P), A647 anti-human CD86 (Sony 2127080), PE anti-human DC-Sign (Sony RT2315020) and APC anti-human CD14 (Sony RT2109040). After a wash, cells were resuspended in PBS and processed on BD Fortessa flow cytometer. Analyses were performed of FlowJo software.

Seahorse XFe 96 analyser experiment. The metabolic assays on MDDC cell culture were performed as previously described[71]. 100,000 cells were harvested at day 5 after transduction and plated in culture medium in 96-well Seahorse plates (Agilent). At day 6, cells were balanced for 1 h in unbuffered XF assay media (Agilent) supplemented for OCR analysis with either 2 mM Glutamine, 10 mM Glucose and 1 mM Sodium Pyruvate or just 2 mM Glutamine for ECAR measurement. Measurements were performed on a Seahorse XFe96 Analyzer (Agilent). For OCR measurements, compounds were injected during the assay at the following final concentrations: Oligomycin (ATP synthase inhibitor, 1 μM), FCCP (uncoupling agent measuring the maximal respiration capacity; 1 μM), Rotenone and Antimycin A (ETC inhibitors; 1 μM). For ECAR measurements, Glucose (10 mM), Oligomycin (1 μM), and 2-Deoxyglucose (2-DG, glycolytic inhibitor; 500 mM) were injected. See Fig. S8 for graphical explanation. For each cell line 4 to 6 technical replicates were evaluated. All OCR and ECAR measurements were normalized to the protein concentration dosed at the end of every experiment.

Quantitative RT–PCR. RNA was extracted from 100,000 cells following the High Pure RNA isolation kit (Roche) instructions. RNA amplification was performed using Taqman primer probes and PCR master mix from ThermoFisher (SAMHD1 #Hs00210019-m1, ISG15 #Hs019211425-s1, SIGLEC1 #Hs00988063-m1, IFI44L #Hs00915292-m1, IFIT1 #Hs01911452-s1, IFI27 #Hs01086370-m1, RSAD2 #Hs00369813-m1) according to the manufacturer's instructions or, for *CLPP* and *Hsp60* transcripts, the fast superior cDNA synthesis with SuperScript IV Vilo Reverse Transcriptase (Invitrogen)[72]. Samples were analyzed on Viia7 Real-Time PCR system (ThermoFisher) and final data were plotted as expression relative to *HPRT*.

Western Blot. 1 million cells were lysed in 100 μL of lysis buffer, composed of protease inhibitor, phosphatase inhibitor and NP40 (Sigma) in MiliQ Water, for 30 min on ice. Concentration of proteins were determined by Pierce BCA assay (ThermoFisher). After centrifugation clearance, 30 μg of protein lysates were boiled at 95 °C for 5 min in DTT and loading buffer (Invitrogen). Lysates were deposit on Bolt SDS page gel (Invitrogen) and transferred on nitrocellulose membrane (ThermoFisher) using Trans Blot Turbo transfert (Biorad). Membranes were saturated with TBS (Euromedex) 0.05% Tween20 (SIGMA) 5% BSA (Euromedex). Membranes were stained with indicated antibodies in TBS 0.05% Tween20 and ECL signal was recorded on Chemidoc (Biorad). The following primary antibodies were used: mouse anti-human Hif1α (BD Pharmingen #610958), mouse anti-human SAMHD1 (Life Technology MA5-25354), rabbit anti-human α-Tubulin (Cell Signaling 2144S) and were revealed using corresponding secondary antibodies anti-mouse HRP (Cell Signaling 7076S) and anti-rabbit HRP (Cell Signaling 7074S). Images were analyzed and band were quantified on ImageJ software.

Cellular indexing of transcriptomes and epitopes by sequencing (CITE-seq) and single cell RNA-sequencing (scRNA-seq). Frozen PBMC of AGS patients or healthy donors (CTRL) were processed by the LabTech single-cell@Imagine facility for cell encapsulation and NGS (Next generation Sequencing). A first experiment on *SAMHD1* deficient patients was performed on PBMC from healthy donors C3 and C5 and on PBMC from patients P7 before treatment and P8_T. A second experiment was performed on PBMC from healthy donors C4 and another vial from C3 and on PBMC from another vial of P7 before treatment (P7_bis) and PBMC from P7 after treatment (P7_T). The scRNA-seq libraries were generated using Chromium Single Cell 3′ Library & Gel Bead Kit v.2 (10x Genomics) according to the manufacturer's protocol. Briefly, cells were counted, diluted at 1,000 cells/μL in PBS + 0,04% and 20,000 cells were loaded in the 10x Chromium Controller to generate single-cell gel-beads in emulsion. After reverse transcription, gel-beads in emulsion were disrupted. Barcoded complementary DNA was isolated and amplified by PCR. Following fragmentation, end repair and A-tailing, sample indexes were added during index PCR. The purified libraries were sequenced on a Novaseq (Illumina) with 26 cycles of read 1, 8 cycles of i7 index and 98 cycles of read 2. Both experiments were integrated together on AGS5 integration, thus including C3, C4, C5, P7, P7_T and P8_T.

Later, an experiment was performed on PBMC from two healthy donors C1 and C2 as well as AGS patients with RNASEH2B mutation (P1 and P2), ADAR1 mutations (P3 and P4) and COPA patients (P5 and P6). On these samples, a CITE-seq protocol was applied to obtain single cell

surface markers expression together with RNA-seq data at the single cell level. First, cells were stained with antibodies tagged with barcodes according manufacturer protocol (Biolegend). The Total-seq B human universal cocktail of antibody from Biolegend was used, the full list is available in supplementary data 2. Following antibody staining, the scRNA-seq libraries were generated using Chromium Single Cell 3′ Library & Gel Bead Kit v.3 (10x Genomics) according to the manufacturer's protocol. The purified libraries were sequenced on a Novaseq (Illumina) with 28 cycles of read 1, 8 cycles of i7 index and 91 cycles of read 2, to reach a sequencing depth of 50000 reads per cell.

During analysis, P8_T, P7, P7_bis and P7_T were grouped together and labeled as "AGS5" group. Similarly, P1 and P2 were grouped as "AGS2", P3 and P4 grouped as "AGS6" and P5 and P6 grouped as "COPA" according mutations present in patients. The integrations with AGS5 samples and the integration AGS/COPA could not be merged due to technical advances (kit 10x for library generation version 2 versus kit version 3) made between experimental setup that do not allow direct comparison. Essentially, the integration AGS2/AGS6/COPA allow significantly more genes to be detected. Moreover, AGS2/AGS6/COPA integration incorporate surface marker expression following CITE-seq protocol were AGS5 integration is limited to scRNA-seq data.

Bulk RNA-seq. MDDC from two healthy donors (MDDC_A and MDDC_B) were transduced with shRNA targeting ADAR, SAMHD1 or RNASEH2B for 6 days. At day 4, 500 μM of DMOG were added in treated conditions. At day6 cells were froze down before RNA extraction using RNA isolation kit from Roche (#11828665001). RNA quality was assessed by capillary electrophoresis using High Sensitivity RNA reagents with the Fragment Analyzer (Agilent Technologies) and the RNA concentration were measured by using both spectrophometry using the Nanodrop and Fragment Analyzer capillary electrophoresis. A sample of MDDC_4 transduced with shSAMHD1 treated with DMOG was planned but the quality controls revealed insufficient quality material to perform the alignment. Total RNAseq stranded libraries (i.e., oriented libraries which enable to know which strand of DNA has been transcribed) were prepared as recommended by the manufacturer starting from ~10 to 20 ng of total RNA using the Stranded Total RNA Prep, Ligation with Ribo-Zero Plus kit (Illumina, kit suitable for total RNA input from 10 ng to 1 μg). An equimolar pool of the final indexed RNA-Seq libraries was prepared and sequenced on a NovaSeq 6000 from Illumina (Paired-End reads 150 bases + 150 bases). A total of ~130 millions of passing filter paired-end reads/clusters was produced per library.

Targeted LC–MS metabolomics analyses. Metabolic analysis was performed on dry cell pellet of AGS patients' PBMC or MDDC at day6 after transduction with shRNA targeting *SAMHD1*, *ADAR* or *RNASEH2B* genes. The extraction solution was composed of 50% methanol, 30% acetonitrile and 20% water. The volume of the extraction solution was adjusted to the cell number (1 ml per 1 × 10E6 cells). After adding the extraction solution, samples were vortexed for 5 min at 4 °C and centrifuged at 16,000 g for 15 min at 4 °C. LC–MS analyses were conducted on a QExactive Plus Orbitrap mass spectrometer equipped with an Ion Max source and a HESI II probe coupled to a Dionex Ulti-Mate 3000 uHPLC system (Thermo). The 5-μl samples were injected into a ZIC-pHILIC column (150 × 2.1 mm; internal diameter 5 μm) with a guard column (20 × 2.1 mm; internal diameter 5 μm) (Millipore) for LC separation. Buffer A was 20 mM ammonium carbonate and 0.1% ammonium hydroxide (pH 9.2) and buffer B was acetonitrile. The chromatographic gradient was run at a flow rate of 0.200 μl min−1 as follows: 0–20 min, linear gradient from 80% to 20% of buffer B; 20–20.5 min, linear gradient from 20% to 80% of buffer B; and 20.5–28 min, 80% buffer B. The mass spectrometer was operated in full-scan, polarity-switching mode with the spray voltage set to 2.5 kV and the heated capillary held at 320 °C. The sheath gas flow was set to 20 units, the auxiliary gas flow to 5 units and the sweep gas flow to 0 units. The metabolites were detected across a mass range of 75–1,000 m/z at a resolution of 35,000 (at 200 m/z) with the automatic gain control target at 10E6 and the maximum injection time at 250 ms. Lock masses were used to ensure mass accuracy below 5 ppm. Data were acquired with Thermo Xcalibur software (Thermo). The peak areas of metabolites were determined using Thermo TraceFinder software (Thermo), identified by the exact mass of each singly charged ion and by the known retention time on the HPLC column. Targeted metabolomics analyses were focused on the small polar compounds in central carbon metabolism.

Bioinformatic analysis. Sequenced reads from libraries generated were demultiplexed and aligned to the human reference genome (hg38), by Institut Imagine bioinformatic facility, using CellRanger Pipeline V6.0. R version 4.1.2 was used for data processing and analysis. Quality control, data integration and downstream analyses were produced using Seurat v4[73]. Apoptotic cells and empty sequencing droplets were removed by filtering cells with low features (nfeatures<500 for AGS/COPA integration and nfeatures<250 for AGS5 and treatment follow up integrations) or a mitochondrial content >20%. Data were normalized using sctransform. For all three integrations generated, the Seurat clustering resolution 1.6 was selected for cluster identification. Labeling of cell types was defined based on expression of curated list of marker genes previously defined[74] together with surface marker expression when available and confirmed by Azimuth automatic labeling of human PBMC[73]. For scRNA-seq datasets DEG were calculated using FindMarker function of Seurat and Bonferroni correction. (DEG lists can be found in Supplementary data 3). For bulk RNA-seq, FASTQ files were mapped to the Human GRCh38/hg38 reference using star and counted by featureCounts from the Subread R package. Analyses were performed using the DESeq2 v1.41 package on R. PCA were calculated on log normalized counts using plotPCA from DESeq2 package. Pathway enrichments were performed by applying the indicated list of DEG on EnrichR software[22] or Ingenuity pathway analysis (IPA, Qiagen)[19]. DEG were selected if fold change > 0.25 and false discovery rate ≤0.05. Enrichment of pathways in the list of DEG were ranked based on combined score. Combined score is a combination of adjusted *p* value and z-score. *p*-value is computed using a standard statistical method used by most enrichment analysis tools: Fisher's exact test or the hypergeometric test. This is a binomial proportion test that assumes a binomial distribution and independence for the probability of any gene belonging to any set. z-score is computed using a modification to Fisher's exact test in which we compute a z-score for deviation from an expected rank. EnrichR has lookup table of expected ranks and variances for each term in the library. These expected values are precomputed using Fisher's exact test for many random input gene sets for each term in the gene set library. EnrichR uses this lookup table to calculate the mean rank and standard deviation from this expected rank as the z-score. Analyses of targeted metabolomic were performed on R, prcomp from R stat package was used for the generation of PCA and extraction of most variable metabolites. Relative expression of each metabolite has been normalised to the median between groups in every analysis.

Gene regulatory network (GRN) inference analysis. To infer GRN, we apply pySCENIC (Single-Cell rEgulatory Network Inference and Clustering)[20] to a compendium of single-cell data from 8 AGS, 2 COPA patients and 6 healthy controls. Firstly, the gene modules that are co-expressed with transcription factors are identified using GRNboost[21]. Secondly, for each co-expressed module, the predicted transcription factor binding motifs and candidate transcription factors for a gene list are identified using *cis-regulatory* motif analyses using *RcisTarget*. To build the final regulons, we merge the inferred target genes of each TF-module that show enrichment of any motif of the given TF. Finally,

regulator-target relationships are extracted and emitted as a set of network edges. Following the above pipeline, we obtain GRN for each sample. To further investigate the TF activity in AGS and control samples collectively, the GRNs of similar samples were integrated using similarity network fusion (SNF)[75] algorithm. The network-fusion step of SNF uses a non-linear method based on message passing theory[76] that iteratively updates every network, making it more similar to the others with every iteration. After a few iterations, SNF converges to a single network. The final network is analyzed and the top 50 TFs in AGS and control GRN were obtained by measuring out-degrees. To understand loss or gain of TF activity in AGS, we then performed differential out-degree analysis (DOA)[77]. DOA scores for the top 50 TFs were obtained by taking the log2 ratio of the number of targets in AGS on the number of targets in control. TFs are then ranked based on absolute value of DOA score.

Cytokine measurement. Supernatant of the MDDC were obtained after centrifugation to remove debris at day 6 after transduction. Cytokines were measured using LEGENDplex Human Anti-Virus Response Panel (Biolegend) following the manufacturer's protocol. Supernatant were not diluted before quantification. Fluorescence was measured on a BD fortessa cytometer.

Confocal microscopy. Cells were seeded on 12 mm ø and 1.5H glass coverslips and fixed in 4% PFA (EMS) for 15 min at RT. Saturation and permeabilization of the samples was performed by incubating the cells for 30 min at RT in PBS-BSA 2.5% supplemented with Triton X-100 0.2%. Primary antibodies against dsRNA (Jena Bioscience), dsDNA (Sigma-Aldrich) and TOMM40 (Proteintech) were diluted at 1/1000 in the saturation solution and incubated with the samples overnight at 4 °C. Secondary antibodies were diluted at 1/1000 in the saturation solution and incubated for 30 min at RT. Nucleus of the cells were stained using a PBS solution containing DAPI (1/10000). The coverslips were then mounted on a glass slide in Prolong Gold antifade reagent (Thermo_P10144). Images were acquired on a Leica SP8_SMD confocal microscope using the x63 oil immersion objective.

Quantification of dsDNA/dsRNA cytosolic dots. Using the ImageJ software, areas of the nuclei of cells were detected using the DAPI channel and the signal contained in the nucleus was removed in all 3 channels of DNA, RNA and mitochondrial staining. The cells were detected individually, and their border were drawn by hand, and the extracellular signal from all channels was discarded. Using a manually set fixed threshold for each channel, the cytosolic dots of RNA and DNA staining were binarized. The mitochondrial signal was binarized as well using a fixed thresholding approach and the nucleic acids dots contained in the detected mitochondrial staining were discarded. The number of remaining dots, considered cytosolic was measured using the 'Analyze Particles' function with the criteria of considering particles only over 10 pixels of size, to limit detection of particles resulting from noise of the signal or of particles partially overlapping with the mitochondrial signal. Fluorescent intensities of the different staining were analyzed using ImageJ.

Quantification and statistical analysis

Statistical analyses were performed on Prism 8.0 (Graphpad) to calculate T statistical tests ***:$p < 0.001$, **:$p < 0.01$, *:$p < 0.05$. The number of unique donors for MDDC generation are listed in figure legends and represent biological replicates. Experiment with lower than 3 replicates were not statistically tested.

Reporting summary

Further information on research design is available in the Nature Portfolio Reporting Summary linked to this article.

Data availability

Raw CITE-seq and scRNA-seq data discussed in this publication have been deposited in NCBI's Gene Expression Omnibus (GEO)[78] and are accessible through GEO Series accession number GSE220764. Processed CITE-seq/scRNA-seq (rds file) and metabolomic data are available in the Figshare database under accession number https://doi.org/10.6084/m9.figshare.31055725. Source data are provided with this paper.

Code availability

Computational code reacquired to reproduce the figures of the paper has been deposited in the Zenodo database under the accession number (https://doi.org/10.5281/zenodo.18229684).

References

1. Rice, G. et al. Heterozygous mutations in TREX1 cause familial chilblain lupus and dominant aicardi-goutières syndrome. *Am. J. Hum. Genet.* **80**, 811–815 (2007).
2. Crow, Y. J. et al. Mutations in genes encoding ribonuclease H2 subunits cause Aicardi-Goutières syndrome and mimic congenital viral brain infection. *Nat. Genet* **38**, 910–916 (2006).
3. Rice, G. I. et al. Mutations involved in Aicardi-Goutières syndrome implicate SAMHD1 as regulator of the innate immune response. *Nat. Genet* **41**, 829–832 (2009).
4. Rice, G. I. et al. Mutations in ADAR1 cause Aicardi-Goutières syndrome associated with a type I interferon signature. *Nat. Genet* **44**, 1243–1248 (2012).
5. Rice, G. I. et al. Gain-of-function mutations in IFIH1 cause a spectrum of human disease phenotypes associated with upregulated type I interferon signaling. *Nat. Genet* **46**, 503–509 (2014).
6. Uggenti, C. et al. cGAS-mediated induction of type I interferon due to inborn errors of histone pre-mRNA processing. *Nat. Genet* **52**, 1364–1372 (2020).
7. Schlee, M. & Hartmann, G. Discriminating self from non-self in nucleic acid sensing. *Nat. Rev. Immunol.* **16**, 566–580 (2016).
8. Tanaka, Y., and Chen, Z. J. STING specifies IRF3 phosphorylation by TBK1 in the cytosolic DNA signaling pathway. *Sci. Signal*. https://doi.org/10.1126/scisignal.2002521 (2012).
9. Crow, Y. J. & Manel, N. Aicardi–Goutières syndrome and the type I interferonopathies. *Nat. Rev. Immunol.* **15**, 429–440 (2015).
10. Van Heteren, J. T. et al. Astrocytes produce interferon-alpha and CXCL10, but not IL-6 or CXCL8, in aicardi-Goutières syndrome. *Glia* **56**, 568–578 (2008).
11. van Marle, G. et al. Human immunodeficiency virus type 1 Nef protein mediates neural cell death: a neurotoxic role for IP-10. 17. https://doi.org/10.1016/j.virol.2004.08.024 (2004).
12. JAK Inhibition in the Aicardi–Goutières Syndrome. *N. Engl. J. Med.* **383**, 2190–2193 (2020).
13. Frémond, M.-L. et al. JAK inhibition in aicardi-goutières syndrome: a monocentric multidisciplinary real-world approach study. *J. Clin. Immunol.* **43**, 1436–1447 (2023).
14. Stoeckius, M. et al. Simultaneous epitope and transcriptome measurement in single cells. *Nat. Methods* **14**, 865–868 (2017).
15. Lepelley, A. et al. Mutations in COPA lead to abnormal trafficking of STING to the Golgi and interferon signaling. *J. Exp. Med.* **217**, e20200600 (2020).
16. De Cevins, C. et al. Single-cell RNA-sequencing of PBMCs from SAVI patients reveals disease-associated monocytes with elevated integrated stress response. *Cell Rep. Med.* **4**, 101333 (2023).
17. Rosenberg, B. R. et al. Genetic variation at IFNL4 influences extrahepatic interferon-stimulated gene expression in chronic HCV patients. *J. Infect. Dis.* **6**, 650–655 (2018).
18. Lee, J. S. et al. Immunophenotyping of COVID-19 and influenza highlights the role of type I interferons in development of severe COVID-19. *Sci. Immunol.* **5**, eabd1554 (2020).

19. Krämer, A., Green, J., Pollard, J. & Tugendreich, S. Causal analysis approaches in Ingenuity Pathway Analysis. *Bioinformatics* **30**, 523–530 (2014).
20. Van de Sande, B. et al. A scalable SCENIC workflow for single-cell gene regulatory network analysis. *Nat. Protoc.* **15**, 2247–2276 (2020).
21. Moerman, T. et al. GRNBoost2 and Arboreto: efficient and scalable inference of gene regulatory networks. *Bioinformatics* **35**, 2159–2161 (2019).
22. Chen, E. Y. et al. Enrichr: interactive and collaborative HTML5 gene list enrichment analysis tool. *BMC Bioinforma.* **14**, 128 (2013).
23. Taylor, C. T. & Scholz, C. C. The effect of HIF on metabolism and immunity. *Nat. Rev. Nephrol.* **18**, 573–587 (2022).
24. Papandreou, I., Cairns, R. A., Fontana, L., Lim, A. L., and Denko, N. C. HIF-1 mediates adaptation to hypoxia by actively down-regulating mitochondrial oxygen consumption. *Cell Metab*. **11**, 187–97 (2006).
25. Zhao, Q. et al. A mitochondrial specific stress response in mammalian cells. *EMBO J.* **21**, 4411–4419 (2002).
26. Martinus, R. D. et al. Selective induction of mitochondrial chaperones in response to loss of the mitochondrial genome. *Eur. J. Biochem.* **240**, 98–103 (1996).
27. Benedetti, C., Haynes, C. M., Yang, Y., Harding, H. P. & Ron, D. Ubiquitin-like protein 5 positively regulates chaperone gene expression in the mitochondrial unfolded protein response. *Genetics* **174**, 229–239 (2006).
28. Holzerova, E. et al. Human thioredoxin 2 deficiency impairs mitochondrial redox homeostasis and causes early-onset neurodegeneration. *Brain* **139**, 346–354 (2016).
29. Brambley, C. A., Marsee, J. D., Halper, N. & Miller, J. M. Characterization of mitochondrial YME1L protease oxidative stress-induced conformational state. *J. Mol. Biol.* **431**, 1250–1266 (2019).
30. Rainbolt, T. K., Atanassova, N., Genereux, J. C. & Wiseman, R. L. Stress-regulated translational attenuation adapts mitochondrial protein import through Tim17A degradation. *Cell Metab.* **18**, 908–919 (2013).
31. Hadjadj, J. et al. Impaired type I interferon activity and inflammatory responses in severe COVID-19 patients. **8**, 718–724 (2020).
32. Leisching, G., Yennemadi, A., Gogan, K. & Keane, J. Interferon α and β induce differential transcriptional and functional metabolic phenotypes in human macrophages and blunt glycolysis in response to antigenic stimuli. *Eur. J. Immunol.* **54**, 2451032 (2024).
33. Reynolds, M. B. et al. Type I interferon governs immunometabolic checkpoints that coordinate inflammation during Staphylococcal infection. *Cell Rep.* **43**, 114607 (2024).
34. Olson, G. S. et al. Type I interferon decreases macrophage energy metabolism during mycobacterial infection. *Cell Rep.* **35**, 109195 (2021).
35. Cunliffe, C. J., Franklin, T. J., Hales, N. J. & Hill, G. B. Novel inhibitors of prolyl 4-hydroxylase. 3. Inhibition by the substrate analog N-oxaloglycine and its derivatives. *J. Med. Chem.* **35**, 2652–2658 (1992).
36. Jaakkola, P. et al. Targeting of HIF-α to the von Hippel-Lindau ubiquitylation complex by O_2 -Regulated Prolyl Hydroxylation. *Science* **292**, 468–472 (2001).
37. Finkel, T. & Holbrook, N. J. Oxidants, oxidative stress and the biology of ageing. *Nature* **408**, 239–247 (2000).
38. Gao, Y. et al. Mitochondrial DNA leakage caused by streptococcus pneumoniae hydrogen peroxide promotes type I IFN expression in lung cells. *Front. Microbiol.* **10**, 630 (2019).
39. Warburg, O. et al. On the Origin of Cancer Cells. *Science* **123**, 7 (1956).
40. Wang, T., Marquardt, C. & Foker, J. Aerobic glycolysis during lymphocyte proliferation. *Nature* **261**, 702–705 (1976).
41. Liang, R. et al. Restraining lysosomal activity preserves hematopoietic stem cell quiescence and potency. *Cell Stem Cell* **26**, 359–376.e7 (2020).
42. Yeh, Y.-H., Yang, Y.-C., Hsieh, M.-Y., Yeh, Y.-C. & Li, T.-K. A negative feedback of the HIF-1α pathway via interferon-stimulated gene 15 and ISGylation. *Clin. Cancer Res.* **19**, 5927–5939 (2013).
43. Ahmed, D. et al. Transcriptional profiling suggests extensive metabolic rewiring of human and mouse macrophages during early interferon alpha responses. *Mediators Inflamm.* **2018**, 1–15 (2018).
44. Pillalamarri, V. et al. Whole-exome sequencing in 415,422 individuals identifies rare variants associated with mitochondrial DNA copy number. *Hum. Genet. Genomics Adv.* **4**, 100147 (2023).
45. Chong, M. et al. GWAS and ExWAS of blood mitochondrial DNA copy number identifies 71 loci and highlights a potential causal role in dementia. *eLife* **11**, e70382 (2022).
46. Liu, C.-S. et al. Oxidative stress-related alteration of the copy number of mitochondrial DNA in human leukocytes. *Free Radic. Res.* **37**, 1307–1317 (2003).
47. Qiu C., et al. Mitochondrial DNA copy number and oxidative DNA damage in placental tissues from gestational diabetes and control pregnancies: a pilot study. *Clin. Lab*. https://doi.org/10.7754/Clin.Lab.2012.120227 (2013).
48. Alkazemi, D., Rahman, A. & Habra, B. Alterations in glutathione redox homeostasis among adolescents with obesity and anemia. *Sci. Rep.* **11**, 3034 (2021).
49. Romeu, M. et al. Evaluation of oxidative stress biomarkers in patients with chronic renal failure: a case control study. *BMC Res Notes* **3**, 20 (2010).
50. Barnérias, C. et al. Respiratory chain deficiency in a female with Aicardi-Goutières syndrome. *Dev. Med Child Neurol.* **48**, 227–230 (2006).
51. Tumienė, B. et al. Inflammatory myopathy in a patient with Aicardi-Goutières syndrome. *Eur. J. Med Genet* **60**, 154–158 (2017).
52. Dragoni, F. et al. Characterization of mitochondrial alterations in aicardi–goutières patients mutated in RNASEH2A and RNASEH2B Genes. *IJMS* **23**, 14482 (2022).
53. Dhir, A. et al. Mitochondrial double-stranded RNA triggers antiviral signalling in humans. *Nature* **560**, 238–242 (2018).
54. Lepelley, A., Wai, T. & Crow, Y. J. Mitochondrial nucleic acid as a driver of pathogenic type I interferon induction in mendelian disease. *Front. Immunol.* **12**, 729763 (2021).
55. Hooftman, A. et al. Macrophage fumarate hydratase restrains mtRNA-mediated interferon production. *Nature* **615**, 490–498 (2023).
56. Swain, A. et al. Comparative evaluation of itaconate and its derivatives reveals divergent inflammasome and type I interferon regulation in macrophages. *Nat. Metab.* **2**, 594–602 (2020).
57. Zhang, W. et al. Lactate is a natural suppressor of RLR signaling by targeting MAVS. *Cell* **178**, 176–189.e15 (2019).
58. Rabinowitz, J. et al. The ability of SAMHD1-deficient monocytes to trigger the type I IFN response depends on cGAS and mitochondrial DNA. *J. Biol. Chem.* **8**, 110430. (2025)
59. Zeng, X. et al. IP-10 mediates selective mononuclear cell accumulation and activation in response to intrapulmonary transgenic expression and during adenovirus-induced pulmonary inflammation. *J. Interferon Cytokine Res* **25**, 103–112 (2005).
60. Yang, J. & Richmond, A. The angiostatic activity of interferon-inducible protein-10/CXCL10 in human melanoma depends on binding to CXCR3 but not to glycosaminoglycan. *Mol. Ther.* **9**, 846–855 (2004).
61. Singh, A. K. et al. Daprodustat for the treatment of anemia in patients not undergoing dialysis. *N. Engl. J. Med* **385**, 2313–2324 (2021).

62. Shutov, E. et al. Roxadustat for the treatment of anemia in chronic kidney disease patients not on dialysis: a Phase 3, randomized, double-blind, placebo-controlled study (ALPS). *Nephrol. Dialysis Transplant.* **36**, 1629–1639 (2021).
63. Steadman, T., and O'Reilly, S. Aberrant fumarate metabolism links interferon release in diffuse systemic sclerosis. *J. Dermatol. Sci.* https://doi.org/10.1016/j.jdermsci.2025.01.002 (2025).
64. Xian, H. et al. Mitochondrial DNA oxidation propagates autoimmunity by enabling plasmacytoid dendritic cells to induce TFH differentiation. *Nat. Immunol.* **26**, 1168–1181 (2025).
65. Rice, G. I. et al. Reverse-transcriptase inhibitors in the Aicardi–Goutières syndrome. *N. Engl. J. Med* **379**, 2275–2277 (2018).
66. Sallusto, F. & Lanzavecchia, A. Efficient presentation of soluble antigen by cultured human dendritic cells is maintained by granulocyte/macrophage colony-stimulating factor plus interleukin 4 and downregulated by tumor necrosis factor alpha. *J. Exp. Med* **179**, 1109–1118 (1994).
67. Mangeot, P.-E. et al. High levels of transduction of human dendritic cells with optimized SIV vectors. *Mol. Ther.* **5**, 283–290 (2002).
68. Manel, N. et al. A cryptic sensor for HIV-1 activates antiviral innate immunity in dendritic cells. *Nature* **467**, 214–217 (2010).
69. Johnson, J. S. et al. Reshaping of the dendritic cell chromatin landscape and interferon pathways during HIV infection. *Cell Host Microbe* **23**, 366–381.e9 (2018).
70. Mangeot, P.-E. et al. Development of minimal lentivirus vectors derived from simian immunodeficiency virus (SIVmac251) and their use for gene transfer into human dendritic cells. *J. Virol.* **74**, 8307–8315 (2000).
71. White, S. M. et al. YAP/TAZ inhibition induces metabolic and signaling rewiring resulting in targetable vulnerabilities in NF2-deficient tumor cells. *Dev. Cell* **49**, 425–443.e9 (2019).
72. Fali, T. et al. Elderly human hematopoietic progenitor cells express cellular senescence markers and are more susceptible to pyroptosis. *JCI Insight* **3**, e95319 (2018).
73. Hao, Y. et al. Integrated analysis of multimodal single-cell data. *Cell* **184**, 3573–3587 (2021).
74. Monaco, G. et al. RNA-seq signatures normalized by mRNA abundance allow absolute deconvolution of human immune cell types. *Cell Rep.* **26**, 1627–1640.e7 (2019).
75. Wang, B. et al. Similarity network fusion for aggregating data types on a genomic scale. *Nat. Methods* **11**, 333–337 (2014).
76. Glass, K., Huttenhower, C., Quackenbush, J. & Yuan, G.-C. Passing messages between biological networks to refine predicted interactions. *PLoS ONE* **8**, e64832 (2013).
77. Lichtblau, Y. et al. Comparative assessment of differential network analysis methods. *Brief Bioinform.* **18**, 837–850 (2016).
78. Edgar, R., Domrachev, M. & Lash, A. E. Gene expression omnibus: NCBI gene expression and hybridization array data repository. *Nucleic Acids Res* **30**, 207–210 (2002).

Acknowledgements

This work was supported by the "*Institut national de la santé et de la recherche médicale*" (INSERM), the Atip-Avenir and "*Emergence ville de Paris*" programs and *Fond de Dotation*, Janssen Horizon and government grants managed by the *Agence Nationale de la Recherche* (ANR) as part of the "investment of the Future" program (*Institut Hospitalo-Universitaire* Imagine grant ANR-10-IAHU-01, Recherche Hospitalo-Universitaire grant ANR-18-RHUS-0010). The Labtech Single-Cell@Imagine is supported by the *Paris Region* and the "*Investissement d'avenir*" program through 2019 ATF funding – *Sésame Filières* PIA (grant 3877871). C.C. is the recipient of a CIFRE PhD (Sanofi). V.G.P. obtained an Imagine international PhD fellowship program supported by the *Fondation Bettencourt Schueller*. B.P. is the recipient of an ANRS post-doctoral fellowship. We thank the Imagine genomics, bioinformatics, cytometry and single-cell core facilities, as well as the metabolic analysis platform from the Necker research institute. Patients' cells were obtained according the research protocol CPP (ID-RCB/ EUDRACT: 2014-A01017-40) and we acknowledge referent physicians, Dr Pierre Meyer (*Neuropédiatrie*, CHU Montpellier), Dr Florence Renaldo (*Neuropédiatrie*, CHU Trousseau, APHP), Dr Claude Cances *Neuropédiatrie*, CHU Toulouse), Pr Nadia Nathan (*Pneumopédiatrie*, CHU Trousseau, APHP), Pr Marie Wislez (*Pneumologie*, CHU Cochin, APHP), Dr Virgine Levrat (*Pédiatrie*, CH Annecy). We acknowledge YJ Crow for help with access to patient material. We wish to thank all patients and their families.

Author contributions

Conceptualization, M.B., M.M.M.; Methodology, M.B., M.M.M.; Formal Analysis, M.B, M.L., S.J., C.C.; Investigation, M.B., I.N., J.L., T.F., A.P., M.Z., V.G.P., F.C.; Resources, B.N., M.L.F., P.Q., M.H., B.B.M, A.B.; Writing - Original Draft, M.B., M.M.M.; Writing – Review and Editing, M.B., M.M.M., B.P., M.L.F., A.L., A.F.; Visualization, M.B., M.L., S.J., C.C.; Supervision, M.M.M., A.F.; Founding Acquisition, M.B, M.M.M.

Competing interests

M.M.M. and M.B. are listed as inventors on a patent application related to this article (Application no. WO2024/165507), entitled "Use of HIF-1 stabilizing agents for the treatment of type I interferonopathies". The remaining authors declare no competing interests.

Additional information

Supplementary information The online version contains supplementary material available at https://doi.org/10.1038/s41467-026-69979-9.

Correspondence and requests for materials should be addressed to Maxime Batignes or Mickaël M. Ménager.

Peer review information *Nature Communications* thanks Navdeep Chandel for their contribution to the peer review of this work. A peer review file is available.

[1]Université Paris Cité, Paris, France. [2]Imagine Institute, Laboratory of Single-cell inflammatory responses and multi-OMICs networks, Atip-Avenir Team, INSERM UMR 1163, Paris, France. [3]Labtech Single-Cell@Imagine, Imagine Institute, INSERM UMR 1163, Paris, France. [4]Platform for Metabolic Analyses, Structure Fédérative de Recherche Necker, INSERM US24/CNRS UAR 3633, F- Paris, France. [5]Asfalia Biologics, ICM, Hôpital Pitié-Salpêtrière, Paris, France. [6]Imagine Institute, Laboratory of neurogenetics and neuroinflammation, INSERM UMR 1163, Paris, France. [7]Genomics Core Facility, Institut Imagine-Structure Fédérative de Recherche Necker, INSERM UMR 1163 et INSERM US24/CNRS UAR3633, Paris Cite University, Paris, France. [8]Pediatric Immuno-hematology and Rheumatology department, Hôpital Necker-Enfants Malades, AP-HP. Centre Université Paris Cité, Reference Centre for Inflammatory Rheumatism, Auto-immune Diseases and Systemic Interferonopathies in Children (RAISE), F-CRIN CRI-IMIDIATE network, Paris, France. [9]Pediatric Neurology Department, Necker–Enfants Malades Hospital, APHP, Paris, France. [10]International Center of Infectiology Research (CIRI), University of Lyon, INSERM U1111, Claude Bernard University, Lyon 1, CNRS, UMR5308, ENS of Lyon, Lyon, France. [11]National Reference Center for Inflammatory Rheumatism, Autoimmune Diseases and Systemic Interferonopathies in Children (RAISE), Pediatric Nephrology, Rheumatology, Dermatology Unit, Hospital of Mother and Child, Hospices Civils of Lyon, Lyon, France. [12]Collège de France, Paris, France. [13]These authors contributed equally: Marine Luka, Surabhi Jagtap, Camille de Cevins.
✉e-mail: maxime.batignes@institutimagine.org; mickael.menager@institutimagine.org